



1

2

## Three different glacier surges at a spot: What satellites observe and what not

3

4

5

6 *Frank Paul<sup>1</sup>, Livia Piermattè<sup>2</sup>, Desirée Treichler<sup>2</sup>, Lin Gilbert<sup>3</sup>, Luc Girod<sup>2</sup>, Andreas Kääh<sup>2</sup>, Ludi-*  
7 *vine Libert<sup>4</sup>, Thomas Nagler<sup>4</sup>, Tazio Strozzi<sup>5</sup>, Jan Wuite<sup>4</sup>*

8

9

10 1 Department of Geography, University of Zurich, 8057 Zurich, Switzerland

11 2 Department of Geosciences, University of Oslo, P.O. Box 1047, 0316 Oslo, Norway

12 3 UCL-MSSL, Department of Space and Climate Physics, Mullard Space Science Laboratory,  
13 Holmbury St Mary, Surrey RH5 6NT, UK

14 4 ENVEO IT GmbH, Fürstenweg 176, 6020 Innsbruck, Austria

15 5 Gamma Remote Sensing, 3073 Gümligen, Switzerland

16

17 Corresponding author: Frank Paul (frank.paul@geo.uzh.ch)

18

19

### 20 **Abstract**

21 In the Karakoram, dozens of glacier surges occurred in the past two decades, making the region  
22 one of its global hotspots. Detailed analyses of dense time series from optical and radar satellite  
23 images revealed a wide range of surge behaviour in this region: from slow advances longer than a  
24 decade at low flow velocities to short, pulse-like advances over one or two years with high veloci-  
25 ties. In this study, we present an analysis of three currently surging glaciers in the central Karako-  
26 ram: North and South Chongtar Glaciers and an unnamed glacier referred to as NN9. All three  
27 glaciers flow towards the same region but differ strongly in surge behaviour. A full suite of satel-  
28 lite sensors and digital elevation models (DEMs) from different sources are used to (a) obtain  
29 comprehensive information about the evolution of the surges from 2000 to 2021 and (b) to com-  
30 pare and evaluate capabilities and limitations of the different satellite sensors for monitoring rela-  
31 tively small glaciers in steep terrain. A strongly contrasting evolution of advance rates and flow  
32 velocities is found, though the elevation change pattern is more similar. For example, South  
33 Chongtar Glacier had short-lived advance rates above 10 km y<sup>-1</sup>, velocities up to 30 m d<sup>-1</sup> and sur-  
34 face elevations increased by 200 m. In contrast, the neighbouring and three times smaller North  
35 Chongtar Glacier had a slow and near linear increase of advance rates (up to 500 m y<sup>-1</sup>), flow ve-  
36 locities below 1 m d<sup>-1</sup> and elevation increases up to 100 m. The even smaller glacier NN9 changed  
37 from a slow advance to a full surge within a year, reaching advance rates higher than 1 km y<sup>-1</sup>. It



38 seems that, despite a similar climatic setting, different surge mechanisms are at play and a transi-  
39 tion from one mechanism to another can occur during a single surge. The sensor inter-comparison  
40 revealed a high agreement across sensors for deriving flow velocities, but limitations are found on  
41 small and narrow glaciers in steep terrain, in particular for Sentinel-1. All investigated DEMs have  
42 the required accuracy to clearly show the volume changes during the surges and elevations from  
43 ICESat-2 ATL06 data fit neatly. We conclude that the available satellite data allow for a compre-  
44 hensive observation of glacier surges from space when combining different sensors to determine  
45 the temporal evolution of length, elevation and velocity changes.

46  
47

## 48 **1. Introduction**

49

50 Glacier surges in the Karakoram are widespread (e.g. Sevestre and Benn, 2015) and have been  
51 thoroughly documented using historic literature sources and time series of satellite images (Cop-  
52 land et al., 2011; Bhambri et al., 2017; Paul, 2020). A large number of publications provides in-  
53 sights into decadal elevation changes (e.g. Bolch et al., 2017; Berthier and Brun, 2019; Brun et al.,  
54 2017; Gardelle et al., 2013; Rankl and Braun, 2016; Zhou et al., 2017) and mean annual flow ve-  
55 locities (e.g. Dehecq et al., 2015; Rankl et al., 2014) at a regional scale. Using various satellite da-  
56 tasetes, several studies have also investigated individual glacier surges at high temporal resolution  
57 (e.g. Bhambri et al., 2020; Mayer et al., 2011; Paul et al., 2017; Quincey et al., 2015; Round et al.,  
58 2017; Steiner et al., 2018).

59

60 This increasing interest is in part due to the hazard potential of glacier surges, in particular when  
61 river damming creates lakes that might catastrophically drain in so-called glacier lake outburst  
62 floods (GLOFs) with far reaching impacts (e.g. Bazai et al., 2021; Bhambri et al., 2019 and refer-  
63 ences therein; Iturrizaga, 2005), but also due to the increased availability of satellite data for char-  
64 acterizing surges in detail (e.g. Dunse et al., 2015; King et al., 2021; Nuth et al., 2019; Rashid et  
65 al., 2020; Wang et al., 2021; Willis et al., 2018). The still limited understanding of surges in the  
66 Karakoram region (e.g. Farinotti et al., 2020) and the high diversity of observed surge characteris-  
67 tics (e.g. Bhambri et al., 2017; Hewitt, 2007; Paul, 2015; Quincey et al., 2015) also contribute to  
68 the recent efforts. These studies found that both main types of glacier surges can be found in the  
69 Karakoram, sometimes side-by-side: The Alaska type, which might be triggered by a change in the  
70 basal hydrologic regime, creates pulse-like surges of a short duration (2-3 years), whereas the  
71 thermally-controlled Svalbard type has often active surge durations of many years (e.g. Jiskoot,  
72 2011; Murray et al., 2002; Raymond, 1987; Sharp, 1988). Although the physical reasons for the  
73 differences and variability of surges in the Karakoram are yet unknown (e.g. glacier properties,  
74 thermal regime, mass balance history), many glaciers in the Karakoram have surged repeatedly,  
75 sometimes at surprisingly constant intervals and over centuries (e.g. Bhambri et al., 2017; Paul,



76 2020). On average, surges in the central Karakoram repeat after 40 to 60 years, but intervals can  
77 range from less than 20 to more than 80 years.

78

79 In the thermally controlled case, it is sometimes difficult to distinguish a regular advance from a  
80 surge, as the transition can be gradual (Lv et al., 2020). Whether an advance (stimulated by a posi-  
81 tive mass budget) is indeed a surge might be determined by comparison with the behaviour of  
82 neighbouring glaciers. As thresholds on advance rates or ice flow speedup might not be efficient to  
83 distinguish (slow) surges from advances in the Karakoram, the typical mass redistribution pattern  
84 of a surge (from an upper reservoir to a lower receiving zone) as obtained from differencing digital  
85 elevation models (DEMs) acquired a few years apart (e.g. Gardelle et al., 2013) is a more reliable  
86 identifier (Lv et al., 2019; Goerlich et al., 2020). Usually, the surface in the upper regions of a  
87 glacier does not lower significantly during a regular advance (Lv et al., 2020). A further method to  
88 discriminate surges from a usual advance is related to a strong increase in crevassing and devel-  
89 opment of shear margins. However, these are only visible in very high-resolution satellite images  
90 or time-series of SAR data (Leclercq et al., 2021).

91

92 In this study, we present (a) a comparative analysis of the on-going surges of three glaciers in the  
93 central Karakoram: North and South Chongtar Glacier and a small, unnamed glacier referred to  
94 here as NN9. We present a comparative analysis of their changes in length, advance rates, flow  
95 velocities and surface elevations to elucidate the respective similarities and differences in surge  
96 behaviour. As a second aim of this study, we (b) investigate the feasibility of various satellite sen-  
97 sors and DEMs to follow the temporal evolution of the surges comprehensively. Included are opti-  
98 cal (Sentinel-2, Landsat, Planet cubesats) and synthetic aperture radar (SAR) imaging sensors  
99 (Sentinel-1, TerraSAR-X), altimeter data from ICESat-2 and DEMs from the Shuttle Radar To-  
100 pography Mission (SRTM), the Satellite Pour l'Observation de la Terre (SPOT), the High Moun-  
101 tain Asia DEM (HMA-DEM) and the Advanced Spaceborne Thermal Emission and reflectance  
102 Radiometer (ASTER) by Hugonnet et al. (2021).

103

104

## 105 **2. Study region**

106

107 The study region is located in the central Karakoram, north of the Baltoro Glacier, at about 5.94°  
108 N and 76.33° E (Fig. 1). East of the study region stands the second highest mountain in the world,  
109 the 8611 m high K2. Slopes of the surrounding terrain are very steep and snow avalanches from  
110 the surrounding rock walls are a major source of glacier nourishment. Mass changes over the past  
111 20 years derived from satellite data using the geodetic method show more or less constant near-  
112 zero mass budgets in the study region (Hugonnet et al., 2021), confirming the continuation of the  
113 'Karakoram Anomaly' (i.e. the balanced mass budgets) in this region (Farinotti et al., 2020).



114

115

*Fig. 1: Overview study region*

116

117 Most precipitation in the study region is brought by westerly air flow during winter, but the mon-  
118 soon brings moist air from the southeast also during summer (Maussion et al., 2014), falling as  
119 snow at the high elevations of the rock walls surrounding most glaciers. However, due to the good  
120 protection from nearly all directions, the amount of snowfall in the study region is limited and a  
121 dry-continental climate can be expected (e.g. Sakai et al., 2015). As surge-type glaciers are abun-  
122 dant (Copland et al., 2011; Bhambri et al., 2017) and repeat intervals are comparably short (Paul,  
123 2020), several glaciers in the Karakoram are typically actively surging at any given time.

124

125 The three glaciers investigated here (North/South Chongtar, NN9) have mean elevations around  
126 5500 m and are surrounded by mountain ridges with elevations between 6000 and 7500 m above  
127 sea level. South Chongtar Glacier (shortened to South Chongtar in the following) is the largest  
128 with an area of  $\sim 31$  km<sup>2</sup> and a length of more than 14 km at minimum extent, but it has a narrow  
129 tongue with a near-constant width of about 800 m. The glacier is mainly east-west oriented in its  
130 upper part, bending towards south-north near the terminus. North Chongtar lies north of South  
131 Chongtar and is connected to it in its accumulation area. It flows from southeast to northwest, co-  
132 vers an area of  $\sim 10$  km<sup>2</sup>, has a length of 4.5 km at minimum extent and is about 400 m wide. The  
133 unnamed glacier NN9 is located on the opposite side of the main valley and flows roughly from  
134 west to east. The glacier is about 3.5 km long at minimum extent with an area of 4 km<sup>2</sup> and a  $\sim 300$   
135 m wide tongue. Table 1 summarises further characteristics and topographic properties.

136

137 *Table 1: Basic properties of the three investigated glaciers*

138

139 At their maximum extent the three glaciers reach Sarpo Laggo Glacier, a compound-basin valley  
140 glacier with a size of 122.3 km<sup>2</sup>. This glacier experienced a massive surge shortly before 1960  
141 (Paul, 2020) and a smaller, more internal one (i.e. not reaching the terminus), between 1993 and  
142 1995 (e.g. Paul, 2015). According to Paul (2020), South Chongtar had a rapid advance during a  
143 surge that started in 1966 with a short active phase of about two years followed by a quiescent  
144 phase with continuous down-wasting and retreat. During this surge it partly compressed the ice  
145 from Sarpo Laggo and deformed a moraine from Moni Glacier (see Fig. 1), leaving an impressive  
146 surge mark. In contrast, North Chongtar started advancing about 55 years ago but has not yet  
147 reached Sarpo Laggo. The Shipton map from 1937 (Shipton, 1938) shows North Chongtar in con-  
148 tact with it, indicating that the terminus might reach it again. The glacier NN9 had its last surge  
149 from about 1961 to 1971 (leaving a small surge mark on Sarpo Laggo) and retreated in its quies-  
150 cent phase until 2000, when it started to advance slowly. The two glaciers to the south of NN9  
151 (NN7 and NN8 in Paul, 2020) both surged around 1955, and again in 1998 and 1980, respectively.





152 NN8 also surged after 2002, indicating a surge cycle of only 20-25 years. The next surge of NN8  
153 can thus be expected soon, at least if environmental conditions prevail.

154

155

### 156 **3. Datasets**

157

158 In this section, we describe the satellite and auxiliary datasets used to derive time series of glacier  
159 outlines, surface flow velocities and elevation changes in the study region. Figure 2 shows the  
160 temporal coverage of each dataset, and the periods selected for the analysis. Changes in glacier  
161 extent have been mapped for the active (advance) phases of the three glaciers, starting with Land-  
162 sat Multispectral Scanner (MSS) images from 1973 for North Chongtar Glacier. The earliest da-  
163 taset used to derive flow velocities and elevation changes were acquired in 2000, the Landsat 7  
164 Enhanced Thematic Mapper plus (ETM+) panchromatic band and the SRTM DEM.

165

166

*Fig. 2: Timeline of datasets used*

167

#### 168 **3.1 Glacier extent and centrelines**

169 We used glacier outlines from the updated Glacier Area Mapping for Discharge from the Asian  
170 Mountains (GAMDAM2) inventory by Sakai (2019) as a starting point for all glacier extents. This  
171 dataset was locally improved (removing rock outcrops and seasonal snow) using a Landsat 8 im-  
172 age acquired on 21 October 2020 (Fig. 1). Given the unknown final length of the glaciers, we dig-  
173 itized possible virtual maximum extents for the three glaciers, avoiding overlapping polygons in  
174 their terminus regions. The virtual extents were guided by maximum extents of previous surges  
175 described by Paul (2020).

176

177 Changes in extent were derived from time series of spatially consistent Landsat data (MSS, TM,  
178 ETM+ and Operational Land Imager (OLI)) from path-row 148-35 as well as a couple of Sentinel-  
179 2 scenes (tile 43SFV) required to bridge sparse cloud-free Landsat scenes after February 2021. The  
180 list of satellite scenes used for determination of geometric changes (outlines, length changes) is  
181 given in Table S1 of the Supplemental Material.

182

183 The centrelines for NN9, South and North Chongtar were manually digitized starting from the  
184 highest points of each glacier down to the virtual maximum extent. The centrelines were divided  
185 into equidistant points of 100 m at which values for velocity and elevation were extracted.

186

#### 187 **3.2. Flow velocity**

188 Time series of optical and SAR data were used to derive glacier flow fields (listed in Table S2).  
189 Landsat 7 and 8 scenes, Sentinel-2 and TerraSAR-X (TSX) were used (Fig. 2) to determine pre-



190 surge flow velocities of South Chongtar and advance/surge phase velocities for all glaciers. Images  
191 from Planet cubesats were used for a comparison of results with Sentinel-2 and some gap filling in  
192 the time series rather than for a full documentation of the active surge of South Chongtar. Velocities  
193 from Landsat 8 were also compared with Sentinel-2.

194

195 From TSX co-registered single-look slant range complex (SSC) images acquired in StripMap  
196 mode, with across- and along-track resolution of up to 3 m are used. The selected image pairs are  
197 from two different tracks, cover the study region in the descending direction and were acquired in  
198 2011, 2012 and 2014 (Table S2). Time series of Sentinel-1 single-look complex (SLC) data ac-  
199 quired in interferometric wide (IW) swath mode were used to test its feasibility to derive flow ve-  
200 locities and to create an animation of the surge that is unobstructed by clouds. The Sentinel-1 IW  
201 SLC data have a nominal ground resolution of 5 m x 20 m.

202

### 203 **3.3 Elevation information**

204 To follow elevation changes of the glaciers before and during the surge, we analysed several  
205 DEMs from both optical and SAR sensors (Table 2). We used the following DEMs with known  
206 acquisition dates: The SRTM1 DEM at 1 arcsec (~30 m) resolution from February 2000 (USGS,  
207 2017), a SPOT5-HRS DEM from January 2010 (Gardelle et al., 2013; we used their version v2 for  
208 rugged areas), a SPOT6 DEM from October 2015 (Berthier and Brun, 2019), and a SPOT7-  
209 derived DEM from October 2020 that was generated for this study. In addition, we used the HMA-  
210 DEM mosaic (Shean, 2017) as a reference for DEM co-registration analysis due to its superior  
211 spatial resolution and accuracy over stable terrain (off-glacier) compared to the other DEMs (Fig.  
212 S1). The HMA-DEM is composed of various DEM datasets mostly acquired during 2015 (Feb.,  
213 April, July, and Aug.) in this region. Elevation values along the centrelines are extracted from these  
214 DEMs and DEM differences are calculated for the periods 2000-2010, 2010-2015 and 2015-  
215 2020. For comparison, we also analysed elevation changes derived from ASTER time series by  
216 Hugonnet et al. (2021). These provide additional information about the 2000-2005 and 2005-2010  
217 period as well as from 2000 to 2019 (before the surge of South Chongtar).

218

219

*Table 2: Overview DEM characteristics*

220

221 We also analysed whether altimetry data from ICESat-2 could be used to reveal elevation changes  
222 at a higher temporal resolution. The Advanced Topographic Laser Altimeter System (ATLAS)  
223 instrument on-board ICESat-2 acquires elevation profiles at a 91-day temporal resolution since  
224 October 2018. Each satellite overpass results in three beam pairs that are separated by 3.3 km and  
225 90 m between/within pairs, respectively (Markus et al., 2017). The ICESat-2 ATL06 dataset pro-  
226 vides geolocated land ice surface heights with 40 m spatial resolution in profile direction. Figure  
227 S2 shows the ATL06 dates and elevations of data points crossing North and South Chongtar, and



228 the two closest repeating pairs of tracks on South Chongtar. Due to the systematic off-pointing at  
229 mid-latitudes, ICESat-2 tracks are not repeated exactly in our study area and the ATL06 data alone  
230 proved too sparse, both geographically and temporally, for further analysis of the surges.

231

232 The ICESat-2 ATL03 Global Geolocated Photon Data (Neumann et al., 2021), from which the  
233 ATL06 dataset is a higher-level derivative, provides surface elevation measurements from individ-  
234 ual photons every 0.7 m along the elevation profiles, revealing details of the surface topography of  
235 the glaciers. The ICESat-2 surface elevations fall into the time gap of the DEMs between 2015 and  
236 2020, thus providing additional temporal information on the surge development. In total, we found  
237 42 intersections with the centrelines of the three investigated glaciers: 23 on South Chongtar (from  
238 seven dates), 13 on North Chongtar (from six dates), and 6 on NN9 (from three dates).

239

240

## 241 **4. Methods**

### 242 **4.1 Glacier extent**

243 The timing of the selected images used to digitize glacier extents varies strongly depending on the  
244 advance rates. To have at least a two-pixel change in frontal position, it varies from several years  
245 for the slow advance of North Chongtar to about 16 days for the surge phase of South Chongtar.  
246 Due to frequent cloud cover, different scenes had to be used for the individual glaciers (Table S1).  
247 For the digitization, the polygon referring to the virtual maximum extent of each glacier was split  
248 into a multi-polygon by digitizing the smaller extents visible on the respective satellite images.

249

250 Length changes between two terminus positions from  $t_1$  and  $t_2$  were derived manually using the  
251 distance tool in ArcGIS. Several values were obtained for each change and a suitable average as-  
252 signed (values usually varied by about  $\pm 10$  m). We only used the Landsat 7 and 8 time series for  
253 this as the Landsat Collection 1 data had a spatial shift compared to Sentinel-2 (e.g. Paul et al.,  
254 2016). The length change values from  $t_1$  to  $t_2$  were divided by the temporal difference ( $t_2 - t_1$ ), con-  
255 verted to mean annual advance rates and assigned to the date that is halfway between  $t_1$  and  $t_2$ .  
256 Cumulative changes were obtained by summing up the individual length changes.

257

### 258 **4.2 Velocities**

259 Flow velocities typically span two to three orders of magnitude, e.g. from  $<0.1$  m  $d^{-1}$  for near stag-  
260 nant glaciers to  $>10$  m  $d^{-1}$  during a surge. When using offset-tracking (e.g. Strozzi et al., 2002) this  
261 range can to some extent be accounted for by varying the search window size or the time between  
262 the acquisition dates of the image pair. If glaciers with very different flow velocities are in the  
263 study region, it might be required to use images from different dates for the analysis or an adaptive  
264 search window (Debella-Gilo and Käab, 2012). In the following, we describe some basics of the  
265 processing lines applied for optical and SAR sensors.



266

267 The normalized cross-correlation algorithm implemented in the correlation image analysis soft-  
268 ware (CIAS, Käab and Vollmer, 2000) is used to calculate the glacier surface displacement be-  
269 tween optical satellite image pairs (Fig. S3 is illustrating the workflow). The satellite images were  
270 not co-registered as we assume that they are corrected for topographic distortion, and therefore the  
271 displacement calculated between two images is the actual horizontal displacement without any  
272 influence of topography. To check co-registration, abundant stable terrain was included in the cor-  
273 relation. The displacements are estimated at a spatial resolution of 100 m while the size of the  
274 search area is set in relation to the maximum displacement estimated between two satellite scenes.  
275 Dividing the displacement by the temporal difference between the image pairs (Table S2) gives  
276 velocity in  $\text{m d}^{-1}$ .

277

278 With optical data, clouds, cast shadows and changes in snow cover lead to false detections or bi-  
279 ased measurements of the calculated displacement fields. These mismatches are removed in post-  
280 processing by setting a threshold of the maximum correlation coefficient ( $<0.5$ ) and velocity. For  
281 Sentinel-2 data, elevated objects such as clouds are detected by applying CIAS between band 4  
282 and band 8 of the same Sentinel-2 scene. The calculated perspective displacements (both bands are  
283 recorded at slightly different positions of the sensor) are then used to mask the clouds. For all sat-  
284 ellite data, spatial filtering based on a moving median window as well as temporal filtering are ap-  
285 plied to remove additional outliers and noise (Fig. S3).

286

287 Surface flow velocities for TSX data were derived by an iterative offset-tracking technique devel-  
288 oped for SAR data (Wuite et al., 2015). This method does not require coherence and is thus also  
289 capable of acquiring flow velocity data over longer time spans and in regions with fast flow. The  
290 method is based on cross-correlation of templates in SAR amplitude images and provides both the  
291 along-track and line-of-sight velocity components from a single image pair. We used a template  
292 size of  $96 \times 96$  pixels for generating velocity maps with 50 m grid spacing and applied a  $9 \times 9$   
293 inverse-distance median filter in the post-processing step to remove outliers and fill in small gaps.  
294 For Sentinel-1, the same method was applied but tests with various image template sizes were per-  
295 formed with an image pair acquired on 4 and 1611. 2020 during the peak of the surge (Fig. S4).

296

### 297 **4.3 Elevation data**

298 We used the MicMac software to generate the SPOT 2020 DEM from the raw imagery (Rupnik et  
299 al., 2017). The pre-processing of all DEMs follows the standard processing steps for DEM differ-  
300 encing. All DEMs were projected to UTM 43N (EPSG 32643), elevations were vertically trans-  
301 formed to the WGS 84 ellipsoid and DEMs were co-registered to the HMA DEM using OPALS  
302 (Pfeifer et al., 2014). Specifically, we applied least squares matching to estimate the full 3D affine  
303 transformation parameters that minimize the errors with respect to the reference DEM over com-



304 mon stable areas. These were manually digitized off-glacier excluding slope values larger than 40  
305 degrees (Fig. S5). We also excluded data voids from further analyses. This removes large parts of  
306 the accumulation areas of some glaciers in the case of the SPOT 2010 and 2015 DEMs, but had  
307 little impact for the other DEMs.

308

309 All DEMs were resampled, clipped and aligned to the same 30 m grid and a high-resolution 5 m  
310 grid for the HMA DEM and SPOT 2020. We did not correct the SRTM DEM for microwave penetra-  
311 tion into ice and snow (Gardelle et al., 2012), as the effect is small and uncertain compared to  
312 the elevation differences caused by the surges. Elevation values were extracted along the centre-  
313 lines and subtracted from SRTM.

314

315 To estimate volume changes resulting from the surges, volume gain and loss (i.e., summing up all  
316 positive and negative values within the tongues) were calculated for each glacier tongue with ad-  
317 justed extents and glacier-specific epochs (Fig. S5). For comparison, we included the glaciers NN7  
318 and NN8 (see Fig. 1) in the analysis as they also surged during the study period.

319

320 As the ICESat-2 ATL06 datasets did not provide useful results, only the ATL03 dataset was fur-  
321 ther processed using python libraries geopandas (Jordahl et al., 2021), rasterio (Gillies et al., 2021)  
322 and shapely (Gillies et al., 2021a). The photon elevations were filtered to only retain elevation  
323 samples classified as likely land or ice surfaces (parameters `signal_conf_ph/signal_conf_ph_landice` >1) and classified into glacier and off-glacier samples using  
324 maximum glacier outlines. On the bright glacier surface, both the weak and strong laser beams  
325 yield sufficient photon returns for complete elevation profiles. This is less true for moraines /  
326 rocky areas (profile 3 in Fig. S6), where the weak beam yields considerably fewer surface returns.

328

329 Elevation values were sampled for all elevation points (containing a DEM cell) and the AMES  
330 stereo pipeline (version 2.7.0, Shean et al., 2016) was used to co-register the elevation profiles (on-  
331 ly off-glacier samples) with the already co-registered DEMs used in this study (no co-registration  
332 offset was found). The profiles were intersected with the glacier centrelines to compare the ATL03  
333 elevation samples with the DEMs. The median of all elevation samples on each profile within a 10  
334 m buffer from the centreline are used as surface elevations at the intersection points.

335

#### 336 **4.4 Uncertainties**

337 The uncertainty of the length change data has been determined by measuring for each glacier and  
338 each time step different points at the terminus. From the range of values, a reasonable mean value  
339 was determined manually. Glacier terminus positions were digitized only once and used only for a  
340 qualitative illustration (outline overlay) of the changes, i.e. we have not explicitly calculated un-  
341 certainties of glacier extents. As a range of sensors with different spatial resolutions is used for the



342 digitizing (e.g. Landsat MSS, ETM+, OLI and Sentinel-2), the uncertainty varies with the sensor.

343

344 Based on the assumption that measurement errors over glaciers and other terrain are common  
345 (Paul et al., 2017), we assessed the uncertainties of glacier flow velocities from stable terrain ve-  
346 locity observations, where flow velocities are supposed to be zero, using the same stable areas as  
347 used for DEM co-registration (Fig. S5). Uncertainties are derived as measures of median and a  
348 robust standard deviation based on the median absolute deviation (MAD), which is a bit less sensi-  
349 tive to outliers (e.g. Dehecq et al., 2015). Co-registration accuracy of the DEMs was computed  
350 from elevation differences calculated over stable terrain (off glacier) with slopes smaller than 40°  
351 (Fig. S5).

352

353

## 354 5. Results

355

### 356 5.1 Changes in glacier extent and morphology

357 In Fig. 3 the temporal evolution of terminus positions is depicted as an overlay of extents showing  
358 slow advances of NN9 (starting in 2000) and North Chongtar (since 1973) along with a rapid ad-  
359 vance of South Chongtar (starting mid-2020). For better visibility, the retreat phase of South  
360 Chongtar from 2000 to mid-2020 is not shown. Snapshots of the geometric evolution can be found  
361 in Fig. S7 for the time period before the surge of South Chongtar (1993-2019) and in Fig. S8 for  
362 the time during its surge (2020-2021). The related cumulative length changes for all three glaciers  
363 are shown in Fig. 4a for their advance phases, whereas Fig. 4b only shows advance rates for the  
364 glaciers NN9 and North Chongtar (they were out of scale for South Chongtar).

365

366

*Fig. 3: Multi-temporal outline overlay advance phase*

367

368 **South Chongtar** entered its quiescent phase after its 1966/67 surge and exhibited constant thin-  
369 ning with limited frontal retreat over several decades. After 30 years (in 2000) the former surge  
370 lobe was still largely ice filled, though increasingly debris covered. Driven by further thinning, a  
371 clear retreat of the terminus (remaining clean ice) became visible after 2000, reaching about -800  
372 m by 2009 and -2300 m by mid-2020. During this retreat phase, its middle part always showed  
373 some residual flow, i.e. it was not completely stagnant. In 1993 a deformation of the medial mo-  
374 raine started moving forward, about 300 m by 2009 and 500 m by 2019.

375

376 In 2017, a new surge developed with the typical funnel-shaped appearance of the front. While the  
377 lowest part of the glacier was still thinning and retreating in 2019, the surge front reached the ter-  
378 minus in July 2020 and the front started advancing by about 3 km in 10 months (Fig. 4a) with ad-  
379 vance rates of up to 12.6 km yr<sup>-1</sup> (35 m d<sup>-1</sup>) in early Nov. 2020. During this time the lower part



380 widened massively and the entire surface became heavily crevassed. The front advanced into its  
381 former surge mark on Sarpo Lago Glacier and pushed the ice surrounding it towards the opposite  
382 side of the valley. By June 2021 advance rates decreased considerably, but the terminus was still  
383 advancing.

384

385

*Fig. 4: Cumulative length changes and advance rates*

386

387 **North Chongtar** on the other hand, advanced at a more or less constant rate of  $30 \text{ m y}^{-1}$  until 2004  
388 when it passed a total of 800 m since 1973 (earliest MSS image, see Table S1). A very high-  
389 resolution satellite image from 2001 is available in Google Earth and shows some crevassing near  
390 the terminus but not a surging glacier. There is no indication of a melt water stream leaving the  
391 glacier snout. After 2005, advance rates increased linearly and we assign this as the onset of the  
392 surge phase. This increase resulted in a nearly completely crevassed surface and widespread shear  
393 margins. Both are also visible in the 15 m resolution Landsat panchromatic bands, and, even bet-  
394 ter, in very high-resolution images from 2011 and 2016 available in Google Earth. In 2013 the  
395 terminus reached a step in the valley slope, creating a deep transverse crevasse that seemed to sep-  
396 arate the lowest part of the tongue but actually didn't. By 2021 nearly the entire surface was still  
397 crevassed and the glacier had advanced by a further 1600 m since 2004, i.e. 2.4 km in total.

398

399 The small valley **glacier NN9** slowly retreated until 1998 and started advancing a year later at  
400 about a constant rate of  $40 \text{ m y}^{-1}$  until 2016 (Fig. 4). Up to this year, its lowest parts had some cre-  
401 vasses but looked otherwise like a usual advancing glacier. This changed a year later when the  
402 glacier thickened considerably, developed shear margins and started advancing at a much higher  
403 rate of up to  $1000 \text{ m y}^{-1}$  in 2021, indicating the start of the surge phase. The increasingly crevassed  
404 surface also became visible in Sentinel-2 images and with the 15 m Landsat 8 band. The total ad-  
405 vance from 1999 to 2018 was 800 m followed by a further 500 m until June 2021. In July the  
406 frontal advance accelerated further reaching nearly  $3 \text{ km y}^{-1}$  in August 2021, whereby the lower  
407 part of the tongue separated from the main glacier and slid down the remaining kilometre in about  
408 a month. More ice is following from higher elevations, possibly leading to some interaction with  
409 the still advancing terminus of South Chongtar.

410

## 411 **5.2 Flow velocities**

### 412 **5.2.1 NN9 and North Chongtar**

413 Selected flow velocity maps for the two glaciers are shown in Fig. 5 and related velocity profiles  
414 along the centreline of the main trunk can be seen in Figs. 6a and b for NN9 and North Chongtar,  
415 respectively. The c. 300-400 m wide tongue of NN9 is at the edge of the possibilities for deriving  
416 flow velocities with offset-tracking (and a 100 m grid) from the optical sensors, but the high reso-  
417 lution of TSX StripMap acquisitions provides near-complete spatial coverage (Fig. 5b). Due to



418 local cloud cover several of the optical image pairs selected for South Chongtar could not be used  
419 for NN9 and North Chongtar.

420

421 Though scattered, the values derived from Landsat 7 (Fig. 5a), Sentinel-2 (Fig. 5c) and Landsat 8  
422 (Fig. 5d) look reasonable. Pre-surge values are around  $0.1 \text{ m d}^{-1}$  with Landsat 7 (2000-2002) and  
423 TSX (2011 and 2012) and a bit higher (up to  $0.2 \text{ m d}^{-1}$ ) with Sentinel-2 in 2017 (Fig. 6a). After-  
424 wards values in the lower part of NN9 (between 2.5 and 4 km) start increasing to  $0.4 \text{ m d}^{-1}$ , reach-  
425 ing  $0.8 \text{ m d}^{-1}$  between August and October 2020. The upper glacier started accelerating in autumn  
426 2020 with a near-linear increase up to the terminus (Fig. 6a), indicating surge activation in the  
427 lower part of the glacier. The increased crevassing of NN9 is also visible in the higher intensity  
428 values of the Sentinel-1 animation towards the latest images (see Supplemental Material).

429

430 *Fig. 5: 2D flow velocity maps 2000-2019 for all glaciers*

431

432

433 For the larger North Chongtar, a slightly better coverage can be obtained from the optical sensors  
434 than for NN9. The most homogenous flow fields are derived by TSX (Fig. 5b) indicating higher  
435 flow velocities of up to  $0.4 \text{ m d}^{-1}$  in its lower two thirds up to the terminus in 2012. The profiles in  
436 Fig. 6b from Landsat 7 show similar values. Velocities derived from Sentinel-2 between 2016 and  
437 2019 are lower in the region from 3 to 5.5 km. There is a zone with very low velocities between  
438 4.5 and 5 km and acceleration afterwards. From August 2019 to October 2020 flow velocities are  
439 between  $0.8$  and  $1 \text{ m d}^{-1}$  near the terminus, indicating that this region is fast flowing and advanc-  
440 ing, whereas the upper regions are still moving with  $0.2$  to  $0.4 \text{ m d}^{-1}$ .

441

442 *Fig. 6: 1D centre-line velocity profiles NN9 & South Chongtar*

443

#### 444 5.2.2 South Chongtar

445 The much larger South Chongtar glacier was adequately captured by the optical sensors so that a  
446 more continuous flow field could be derived (Fig. 5) and pre-surge flow evolution could be fol-  
447 lowed in detail (Fig. 7a). Comparing the maps in Fig. 5, a slow but steady increase of flow veloci-  
448 ties from 2000 to mid-2019 over large parts of the glacier can be seen, starting at about  $0.15 \text{ m d}^{-1}$   
449 and ending at  $0.4 \text{ m d}^{-1}$ . These values are similar to the other two glaciers, but affect a larger re-  
450 gion. The temporal evolution shown in Fig. 7a confirm this observation, pre-surge flow velocities  
451 are highest (up to  $0.2 \text{ m d}^{-1}$ ) near the middle of the glacier (around 8 to 10 km) and decrease gradu-  
452 ally to  $0 \text{ m d}^{-1}$  at its highest and lowest points. In the region between 11 and 14 km the gradual in-  
453 crease of flow velocities can be followed from 2000/02 (with Landsat 7) to 2014 (with TSX).  
454 Mean annual values with Landsat 8 from 2013 to 2014 match perfectly with mean monthly TSX  
455 values from April to May 2014. Landsat 8 velocities from 2013 to 2016 and Sentinel-2 from 2016





456 to 2019 show the continuation of the slow velocity increase over the entire glacier length, reaching  
457  $0.4 \text{ m d}^{-1}$  in 2018/19. A direct comparison with Landsat 8 over nearly the same period (grey dots in  
458 Fig. 7a) is shown on top of the curve from Sentinel-2, indicating again a near-perfect match. In  
459 August 2019 the gradual increase changed at first rapidly to  $0.8 \text{ m d}^{-1}$  and then more slowly to  $1.1$   
460  $\text{m d}^{-1}$  between September 2019 and June 2020. With the stagnant terminus still at 13.5 km, the  
461 strong velocity increase behind the front marks the onset of the surge around August 2019.

462

463 *Fig. 7: Velocities South Chongtar*

464

465 The last curve from Fig. 7a is repeated in Fig. 7b (dark blue at the bottom), as we had to switch the  
466 scale for better visibility of velocities during the surge phase. Flow velocities increased to about 4  
467  $\text{m d}^{-1}$  by July 2020. In August 2020 we could derive detailed flow fields from Sentinel-2 images  
468 acquired only 5 days apart. A sharp surge front with maximum velocities formed, reaching values  
469 of more than  $25 \text{ m d}^{-1}$  in August/September 2020. With peak velocities near  $30 \text{ m d}^{-1}$  as derived  
470 locally from Planet imagery (Fig. S9), South Chongtar Glacier had likely one of the highest flow  
471 velocities ever measured in the Karakoram region. Behind this maximum, flow velocities de-  
472 creased about linearly back to 3 km along the centre line. When the surge front reached the termi-  
473 nus in July 2020, a rapid advance started (see 5.1). Velocities dropped to  $15 \text{ m d}^{-1}$  by November  
474 2020 and below  $10 \text{ m d}^{-1}$  by January 2021. Afterwards, maximum velocities near km 15 changed  
475 only slowly over the entire glacier length, indicating that the active surge was on-going. Around 10  
476 km along the centre line, velocity is still around  $5 \text{ m d}^{-1}$  in early May 2021 or 40 times higher than  
477 during the quiescent phase (Fig. 7b). The related Hovmöller diagram for the surge phase in Fig. 7c  
478 confirms the strong pulse-like acceleration in August 2020 with a rapid decline afterwards. The  
479 corresponding 2D plots of flow velocities during the surge phase of South Chongtar (Fig. 8) also  
480 reveal the rapid velocity increase by September 2020 and the decrease afterwards.

481

482 *Fig. 8: 2D maps of surface velocities South Chongtar*

483

484 The spatial distribution of highest flow velocities of Figs. 8b and c are not symmetric to the centre  
485 line, indicating that the deformation-related maximum flow velocity in the centre of a glacier has  
486 reduced relevance here. This somehow counterintuitive behaviour indicates that during a surge  
487 basal sliding is the process dominating over deformation. Other possibilities are a decreased re-  
488 sistance of the valley floor or because of the topography redirecting the mass flow from northwest  
489 to north. The cross-profile flow velocities (Fig. 9) reveal that this pattern persists throughout the  
490 entire surge.

491

492 *Fig. 9: 1D cross-profile velocities South Chongtar (surge phase)*

493



494 **5.3 Elevation changes**

495 In the three panels of Fig. 10 we show differences in elevation between the SRTM DEM and the  
496 other four DEMs along the centrelines of the three glaciers. Additionally, differences from selected  
497 ICESat-2 ATL03 points are plotted. Figure 11 shows related elevation change maps for 2000 –  
498 2010, 2010 – 2015, 2015 – 2020 and 2000 – 2020. DEM differences obtained from ASTER in an  
499 independent study (Hugonnet et al., 2021) have been used for comparison.

500

501 The elevation data for **NN9** (Fig. 10a) show virtually no change in its upper part down to 3.5 km  
502 where the terminus was located in 2000. The ICESat-2 data adds no further information here, as all  
503 available data points are located in the upper part. Below this region, the ‘elevation gain’ due to  
504 the advancing snout can be followed down to km 4.5 in 2020. The small region of elevation gain  
505 by the advancing tongue is also visible in each of the maps in Fig. 11. The elevation differences  
506 between the two high-resolution DEMs from 2015 and 2020 in Fig. 11c reveal some surface low-  
507 ering in the upper part, but over the longer period 2000 to 2020 (Fig. 11d) this lowering nearly dis-  
508 appears (i.e. is smaller than the SRTM uncertainty). So for NN9 the typical mass transfer of a  
509 surge could not be observed until October 2020 and elevation changes look like expected for a  
510 usual advance rather than a surge.

511

512 For **North Chongtar** (Fig. 10b) the situation is similar, but a surface lowering of about 40 m can  
513 be observed at higher elevation. The SPOT data from October 2015 and ICESat-2 data points from  
514 December 2018 at 4.2 km indicate that the largest changes happened between 2015 and 2018. Ac-  
515 cordingly, this change is well visible in the high-resolution 2015-2020 DEM difference (Fig. 11c)  
516 and the differences over the full 2000-2020 period (Fig. 11d). However, also here the elevation  
517 gain in the lower glacier part is comparably localized and largely due to the advance of the termi-  
518 nus.

519

520 *Fig. 10: 1D profile elevation changes compared to SRTM*

521

522 **South Chongtar** shows profiles (Fig. 10c) and surface change patterns (Fig. 11) that are in line  
523 with a typical surge, maybe apart from the fact that the thickening of the upper glacier regions is  
524 limited. The 2000 to 2010 change map (Fig. 11a) shows a slightly bluish upper part and some arte-  
525 facts. Over the longer 2000 to 2015 period the elevation gain from 4 to 12 km is about 20-30 m  
526 (Fig. 10c), but further down a significant surface lowering (>50 m) can be observed between 13  
527 and 18 km. This lowering is also visible in the 2D map of Fig. 11a, marking at its upper point the  
528 position where the active ice starts, i.e. where the surface lowering is compensated by the mass  
529 flux. The 2020 surge moved ice between 3 and 8 km towards its lower part between 10 and 16 km,  
530 causing a surface elevation decrease of 20-40 m in the reservoir zone and an increase of up to 130  
531 m at km 14.



532

533 The ICESat-2 data points constrain the surface elevation evolution in time (Fig. 10c): The tongue  
534 was still only slightly thicker at 12 km in March 2019, as surface lowering of the upper part (at 5.7  
535 km) had not started in February 2020 and the terminus had not advanced by March 2020. Between  
536 6 and 14 km we find a smooth linear increase of the elevation differences (Fig. 10c) - but the ICE-  
537 Sat-2 data points at 9.5 km show a slight surface lowering between December 2019 and August  
538 2020, indicating that the surge front passed this part of the glacier already before the end of August  
539 2000. The 2015 to 2020 elevation change map (Fig. 11c) reveals that elevation changes mostly  
540 occurred over this time period. Due to the opposite elevation change pattern before 2015, elevation  
541 changes over the full period 2000-2020 are less pronounced. The constantly down-wasting Sarpo  
542 Laggo Glacier in the valley floor shows an elevation loss of up to 100 m over this period.

543

544

*Fig. 11: 2D elevation change maps*

545

#### 546 **5.4 Volume changes**

547 In Table 3 the results of the calculated volume changes are listed, differentiated for the gain and  
548 loss part. They add some quantitative information over a larger part of the glacier surface (see Fig.  
549 S5). With the timing of the DEMs not always synchronous with the start/end of a surge, the calcu-  
550 lated values can be underestimated due to the overlap of surge phases. For example, the volume  
551 gain in the lower part of South Chongtar from 2000 to 2020 includes the volume loss between  
552 2000 and 2019. For this reason we only analyse the 2015 to 2020 changes for South Chongtar

553

554 For NN9 no mass transfer from an upper region is found. We have a near zero mass loss compared  
555 to a clear volume gain of  $0.03 \text{ km}^3$ . For the continuous advance/surge of North Chongtar the vol-  
556 ume gain is a bit higher than the loss resulting in a small overall volume gain over the full 20-year  
557 period (Fig. 11d). However, Fig. 11c reveals that compensation effects are included. Between  
558 2015 and 2020 some of the volume gain from the period before has already started thinning. The  
559 volume gain part for South Chongtar is about 10 times higher compared to North Chongtar and  
560 NN9. However, there is also considerable volume loss at higher elevations compensating about  
561 half of the gain. To put just the volume gains of these five glaciers ( $+0.46 \text{ km}^3$ ) into perspective,  
562 the (uncompensated) volume loss of Sarpo Laggo Glacier over the full period ( $-0.47 \text{ km}^3$ ) is the  
563 same.

564

565

*Table 3: Volume changes*

566

#### 567 **5.5 Sensor intercomparison**

##### 568 **5.5.1 Velocities**

569 As can be seen in Fig. 7a, velocity values derived from the 15 m resolution Landsat 8 panchro-



570 matic band for the period July 2018 to July 2019 are the same as from 10 m resolution Sentinel-2  
571 data for the period August 2018 to August 2019. Both lines are basically on top of each other and  
572 the average differences are insignificant. The same applies to TSX velocities from April to May  
573 2014 compared to annual mean values from Landsat 8 over the July 2013 to July 2014 period, the  
574 latter curve being on top of TSX in Fig. 7a (apart from the region between 8 and 9 km).

575

576 The Planet cubesat images cover only the lower part of the glacier. Here, the Planet velocity (Fig.  
577 S9) reveals the same increase/decrease pattern as the Sentinel-2 velocity profile (Fig. 7b). Direct  
578 comparison of flow velocities reveals only small differences (Fig. S10) that can be related to  
579 slightly different time intervals. This is different when comparing Sentinel-1 derived velocities  
580 with Sentinel-2 (Fig. S11). The large image template sizes of 128 x 64 (450 m x 900 m) for South  
581 Chongtar (tongue width 800 m) result in a strong underestimation of Sentinel-1 velocities with  
582 errors much greater than those indicated in previous studies for larger Arctic glaciers (Paul et al.,  
583 2017; Strozzi et al., 2017). The density of the information is also very low compared to Sentinel-2,  
584 indicating that Sentinel-1 data do not reveal sufficient detail about the surge.

585

### 586 **5.5.2 Elevation changes**

587 Of the seven analysed elevation datasets, ICESat-2 elevation profiles show most detail compared  
588 to the DEMs and is also resolving small surface features such as crevasses and séracs (Fig. S6).  
589 Both the weak and the strong laser beams of ICESat-2's three beam pairs provide equally good  
590 data in the snow-covered accumulation areas (top panels in Fig. S6). On darker and more rugged  
591 surfaces the weak beam yields considerably fewer photon returns than the strong beam (bottom  
592 panels in Fig. S6).

593

594 Elevation differences between the HMA DEM and the SPOT DEM from 2015 are depicted in Fig.  
595 S12. A small advance of North Chongtar and a slight elevation increase on South Chongtar within  
596 the few months' time gap is visible. The latter is confirmed by the cross transects in the middle  
597 panels in Fig. S6. In contrast, the elevations of the two 2015 DEMs agree very well for the tran-  
598 sects in the upper accumulation area (top panels) and the down-wasting tongue in the main valley  
599 (bottom panels). Apart from artefacts and local differences in very steep terrain, elevations of the  
600 DEMs from 2015 agree very well both on and off glaciers.

601

602 The elevation changes derived from the ASTER DEM time series by Hugonnet et al. (2021)  
603 shown in Fig. S13 are similar to the time series we analysed from SRTM, SPOT and the HMA  
604 DEMs (Fig. 11). The ASTER DEMs have more artefacts and local differences, in particular in  
605 very steep terrain. In contrast, the strong spatial filtering inherent in the ASTER dataset, smooth-  
606 ens artefacts and data gaps off and to some degree also details on glaciers. Locally, the ASTER  
607 data set is less complete, e.g., the advance of North Chongtar is not well covered and the advance



608 of the glacier NN8 is not visible.

609

610 There are no further insights when splitting the 2000-2010 period into a 2000-2004 and 2005-2009  
611 period, but the 2000 to 2019 period from ASTER (Fig. S13f) reveals the up to 40 m elevation in-  
612 crease in the upper region of South Chongtar. This ‘reservoir zone’ seemingly stretches over the  
613 entire upper glacier rather than being an isolated region. In 2019 the surge has not started, so the  
614 strong elevation loss in its lower part from post surge down-wasting is also very prominent. Eleva-  
615 tion gain from 2000 to 2019 is also visible for the upper part of Sarpo Laggo Glacier and the lower  
616 part of Moni Glacier.

617

## 618 **5.6 Uncertainty assessment**

### 619 **5.6.1 Glacier length changes**

620 Uncertainties of the length changes are estimated to be in the order of one image pixel, i.e. 60 m  
621 for MSS, 30 m for TM, 15 m for OLI pan and 10 m for Sentinel-2. As frontal advances have only  
622 been measured for a change of at least 3 to 4 pixels, the given values should be well outside the  
623 uncertainty range in most cases. However, the calculated frontal advance rates for glacier NN9 and  
624 North Chongtar (Fig. 4b) show fluctuations. These can be attributed to the measurement uncertain-  
625 ties so that in reality the increase might have been smoother and more gradual. There is thus some  
626 caution to not over-interpret the details of the change rates.

627

### 628 **5.6.2 Flow velocities**

629 The displacements measured by Landsat over the selected stable areas show median values close  
630 to the expected value of 0 m d<sup>-1</sup>, with a MAD between 0.01 and 0.04 m d<sup>-1</sup>, as reported in Table S2.  
631 Among the Landsat data, Landsat 7 shows the smallest standard deviation based on the MAD. For  
632 Sentinel-2, the uncertainties of the displacement on stable terrain are lower for the pairs with a  
633 time interval of approximately a year. For these pairs, the median and the MAD of the velocity are  
634 of the same order of magnitude as the Landsat results. For shorter time intervals (5 to 45 days), the  
635 Sentinel-2 velocity shows medians between 0.15 and 1.58 m d<sup>-1</sup> with a maximum MAD of 1.39 m  
636 d<sup>-1</sup>. Displacement from Planet data gives the largest error with medians and MAD values ranging  
637 from 0.3 m d<sup>-1</sup> to 2.50 m d<sup>-1</sup>. One pair showed a significantly higher error with a median value of  
638 8.64 m d<sup>-1</sup> and a corresponding MAD value of 4.76 m d<sup>-1</sup>, which is in a similar order of magnitude  
639 to the displacement measured in the centre line of the glacier (13.89 m d<sup>-1</sup>). TSX revealed the low-  
640 est uncertainty with values of both median and MAD close to 0 m d<sup>-1</sup>.

641

### 642 **5.6.3 Elevation data**

643 The median elevation differences to the reference DEM (HMA DEM) are 1.02 m (SRTM), 1.03 m  
644 (SPOT 2010), -0.12 m (SPOT 2015) and 1.08 m (SPOT 2020), with standard deviations of 3-15 m  
645 (Table S3). Also mean elevation differences, which are more sensitive to extreme values, are <1.4



646 m for all DEM difference pairs except for the SPOT 2020-SRTM2000 DEM pair ( $2.4 \pm 8.8$  m).  
647 These are small differences and fully within the range of expected uncertainties (after successful  
648 co-registration), considering the very steep and rugged terrain. We found no indication of remain-  
649 ing horizontal shifts between the DEMs (this would be visible as an aspect-dependent pattern in  
650 Fig. 11). The comparison of the SPOT 2015 and HMA 2015 DEM (Fig. S12) shows a minor tiling  
651 effect caused by the composite nature of the HMA DEM in the upper accumulation areas of North  
652 and South Chongtar. The mean uncertainty of the ATL06 ICESat-2 data was  $\pm 5.37$  m. However,  
653 we assume that ATL03 elevation uncertainties are in the order of decimetres on the relatively  
654 smooth glacier surface.

655

656

## 657 **6. Discussion**

658

### 659 **6.1 Interpretation of the surges**

660 The contrasting surge behaviour of North and South Chongtar glacier is remarkable as the two  
661 glaciers with the likely highest (South Chongtar) and lowest (North Chongtar) flow velocities and  
662 advance rates during a surge (in the entire Karakoram) can be found side-by-side. At first glance it  
663 seems that the sudden and short-lived surge of South Chongtar is hydrologically controlled (Alas-  
664 ka type), whereas the neighbouring North Chongtar surge seems thermally controlled (Svalbard  
665 type). However, as Quincey et al. (2015) noted, this simplified picture does not hold for many  
666 glacier surges in the Karakoram, which often show characteristics of both types. For example, the  
667 South Chongtar surge reached its maximum flow velocities in summer rather than winter and their  
668 drop is very slow rather than fast. Moreover, flow velocities increased slowly, constantly and over  
669 large parts of the glacier rather than being located at a clearly localized surge front. These observa-  
670 tions better fit to a thermally controlled surge and implies that both mechanisms apply and the  
671 surge mechanism could be named ‘hybrid’.

672

673 The slow and near constant advance of North Chongtar and NN9 might not even be classified as a  
674 surge, but given that both glaciers also developed nearly all characteristics of a surge at some  
675 point, the former advance phase might be seen as a part of the surge. Still, from the evolution of  
676 advance rates or flow velocities alone it is nearly impossible to pin down the exact surge onset for  
677 North Chongtar. Morphological changes (heavy crevassing, shear margins) indicate that this might  
678 have happened around 2010, but considering the near linear increase of advance rates after 1996,  
679 one might assign the onset also to that year. In any case, the more or less constant advance for  
680 more than 30 years before 1996 is exceptional and only comparable to the very slow advance of  
681 Maedan Glacier in the neighbouring Panmah region that also started in the 1960s, before advance  
682 rates considerably increased in the mid-1990s and the glacier started surging (Bhambri et al. 2017;  
683 Paul, 2020). Such prolonged advances might also be a consequence of a positive mass balance that



684 one glacier converted to a continuous advance and another one to a surge (Lv et al., 2020). At least  
685 the elevation change pattern of North Chongtar over the 2000-2020 period reveals a clear and typi-  
686 cal redistribution of mass from a higher reservoir zone to a lower receiving zone.

687  
688 This is different for NN9, which only shows elevation increase in its lower part over this period  
689 without any measurable surface lowering higher up. This rather unique criterion for surge identifi-  
690 cation fails here and would exclude the glacier from being surge type. However, a different im-  
691 pression emerges when looking at the temporal evolution of advance rates and flow velocities. In  
692 2016 the former increased considerably from about 40 m y<sup>-1</sup> to more than 1 km y<sup>-1</sup> and the mor-  
693 phology of the surface changed from rather smooth to highly crevassed. Measurable flow veloci-  
694 ties increased in 2019 from 0.2 to 0.8 m y<sup>-1</sup> and the Landsat 8 image pair from 2018 to 2019 (Fig.  
695 5d) also reveals an increase. With its recent rapid advance, the glacier has now reached its former  
696 1971 maximum extent and also looks the same in terms of a completely crevassed surface (Paul,  
697 2020). The slow advance might have resulted from a positive mass balance but could also be a  
698 thermally controlled surge. However, the recent increase in advance rates could also be due to a  
699 hydrologically controlled surge and/or due to the steep slope and dynamic effects. Compared to  
700 North Chongtar, the switch from advance to surge occurred much more sudden.

701  
702 For South Chongtar the situation is clearer as its rapid advance and more than 100-fold increase in  
703 flow velocities (from 0.2 to more than 25 m/d) is typical for a hydrologically controlled surge with  
704 increasing basal water pressure. We assume that its thin lowest part was frozen to the bed (e.g.  
705 Obu et al., 2019), effectively blocking water release for some time. The interesting points of the  
706 current surge are: (a) the gradual increase of flow velocities in the region above its fixed terminus  
707 (at 13.5 km), (b) the extreme velocity increase from July to September 2020, (c) the high maxi-  
708 mum velocities of 30 m d<sup>-1</sup>, (d) the location of the maximum away from the centre, and (e) the  
709 more or less constantly high flow velocities over large parts of its length from January to May  
710 2021. The latter is responsible for the ongoing mass transport and advance of the terminus and im-  
711 plies that basically the entire glacier was activated by the surge. As mentioned above, points (a)  
712 and (e) are more typical for thermally controlled surges so with both characteristics this surge can  
713 be classified as hybrid. That velocities increase from the centre to the boundary of a glacier (Fig.  
714 9) is likely rather unique. We assume this is caused by the surrounding topography, i.e. the change  
715 of flow direction from northwest to north imposed by the mountain walls. The centre of the ad-  
716 vancing terminus collided with the southern rock wall and was then diverted to a different direc-  
717 tion. As the glacier was likely sliding over its full width, the resistance at the boundaries was likely  
718 limited.

719  
720 Maximum surface flow velocities of 30 m d<sup>-1</sup> are only visible with Planet and to the edge of the  
721 glacier (Fig. 9), Sentinel-2 values peak at 27 m d<sup>-1</sup>. This is likely due to the higher resolution of



722 Planet compared to Sentinel-2 and hence to the smaller region used for spatial averaging. Also the  
723 shorter time period considered (3 days) might play a role. Whereas high flow velocities of about  
724  $15 \text{ m d}^{-1}$  have been reported previously (Quincey et al., 2015; Paul et al., 2017; Bhambri et al.,  
725 2020), values above  $25 \text{ m d}^{-1}$  are only rarely observed in the Karakoram (Rashid et al., 2020). The  
726 latter study reports values near  $50 \text{ m d}^{-1}$  for the last surge of Shispar Glacier (derived from 3 m  
727 Planet data), but the flow fields look a bit ‘bumpy’ and image processing artefacts might have con-  
728 tributed to the high values. We assume that the rapid increase in flow velocities during Ju-  
729 ly/August was due to additional lubrication from summer surface melt water.

730

731 In principle, a surge simply moves mass downstream implying that the net volume change should  
732 be about zero. However, if surges take place over very long periods (>5 years) there will also be a  
733 signal from the usual ablation and accumulation. Moreover, for DEMs derived from optical sen-  
734 sors problems in snow covered or steep terrain (shadow) exists that might create data gaps in the  
735 region where the mass has been removed (or where mass gain took place before a surge). Both  
736 effects can create biases leading to over- or underestimation of calculated volume changes. These  
737 apply also to the changes calculated over ten-year periods and the SPOT DEM from 2010 that had  
738 data voids in the steep upper regions of some glaciers. In consequence, volume changes calculated  
739 with this DEM are incomplete and need to be interpreted with care. However, as both positive and  
740 negative changes take place in regions of increased uncertainty, the net effect is likely small.

741

## 742 **6.2 Sensor capabilities and limits**

743 The sensor intercomparison revealed a very good agreement between the velocity data derived  
744 from TSX StripMap mode and Sentinel-2 with Landsat 8 (Fig. 7a), as well as between Sentinel-2  
745 and Planet (Fig. S10). This confirms that all three optical sensors can be used to derive the tem-  
746 poral evolution of flow velocities – cloud cover, snow conditions and cast shadow permitting. The  
747 key point is the choice of the temporal baseline of image pairs as a function of glacier surface  
748 changes, sensor resolution and the targeted velocity field. At  $20 \text{ m d}^{-1}$  a 5 (3) day interval is equiv-  
749 alent to a change by 10 pixels with Sentinel-2 (20 with Planet in 3 days). At  $0.1 \text{ m d}^{-1}$  the dis-  
750 placement is about 35 m (3 Sentinel-2 pixels) after a year, which is at the lower end of what is de-  
751 tectable with offset-tracking.

752

753 Unfortunately, Sentinel-1 performed poorly on South Chongtar, mostly due to the fact that it is a  
754 narrow tongue (width less than 800 m) situated between steep mountain flanks. Because of the  
755 relative large size needed for the matching window (Fig. S4), too many non-moving off-glacier  
756 pixels are included affecting the velocity retrieval considerably (Fig. S11). Also, the large and fast  
757 surface changes on the rapidly surging glacier might have changed the backscatter patterns too  
758 much to be tracked over time (Strozzi et al., 2017). The minimum width of a glacier to be reliable  
759 monitored with Sentinel-1 in the Himalayas is likely around 2 km. On the contrary, TSX yielded





760 dense and consistent velocity values for all three glaciers (pre-surge-phase). As it seems, the map  
761 in Fig. 5b captures nicely the flow acceleration of North Chongtar in 2012, which decreased after-  
762 wards (Fig. 6b). The much noisier values from Landsat 8 in this figure (compared to Sentinel-2  
763 and TSX) revealed that the 15 m resolution of the Landsat panchromatic band is seemingly insuf-  
764 ficient to track displacements precisely. Note, though, that these comparisons are not strictly as the  
765 sensors have different resolutions, and the datasets cover different phases of the surges and thus  
766 different surface conditions.

767

768 The compared DEMs are of similar quality over glaciers, but the SPOT 2010 DEM used by  
769 Gardelle et al. (2013) suffered from strong artefacts at steep slopes. The elevation values of the  
770 SPOT 2015 and HMA DEM (which is also from 2015 in this region) are basically identical apart  
771 from individual raster cells. So elevation changes from 2000 (SRTM) to 2015 (HMA DEM) can  
772 also be derived from freely available DEMs. The SPOT 2020 DEM is of superb quality but the  
773 raw image pair had to be purchased. For a study looking at specific glaciers this is certainly  
774 worthwhile, but does typically hamper larger regions to be covered.

775

776 The surface elevation detail and accuracy of the freely available ICESat-2 ATL03 photon data sur-  
777 passes all other datasets, including the SPOT 2020 DEM (Fig. S6). When combined with one or  
778 several DEMs, the higher temporal resolution provides additional information on how the eleva-  
779 tion changed in-between DEM time stamps. This may be very useful for slower changes or to fur-  
780 ther constrain the onset/end of a rapid change, such as a surge. However, ICESat-2 only provides  
781 elevation profiles with varying locations, which makes this data type more demanding to analyse.  
782 The footprints of the ICESat-2 ATL06 time series alone are too sparse to derive any useful trends  
783 in glacier surface elevation.

784

785 The DEM time series from ASTER images (Fig. S13) derived by Hugonnet et al. (2021) shows the  
786 same trends as from the DEMs used here. They provide further information over the 2000–2005  
787 and 2005–2010 periods, but miss the surge of South Chongtar as they end in 2019. On the other  
788 hand, they cover a much larger area and clearly reveal the increase in surface elevation of South  
789 Chongtar over the full 2000–2019 period. The coverage of the smaller glaciers is noisier with AS-  
790 TER than with the DEMs we have used and locally values are missing, but the temporal evolution  
791 over several larger glaciers can be well followed. Deriving further DEMs from future ASTER ste-  
792 reo scenes might thus help to determine total volume changes after all surges have come to an end,  
793 including the yet not visible volume loss in the reservoir zone of NN9.

794

### 795 **6.3 Uncertainties**

796 The one-pixel uncertainty in deriving terminus positions and length changes translates into an un-  
797 certainty of the calculated advance rates. How large the uncertainties are, depends on the sensor



798 resolution and the time period between two measurements. It is assumed that at least a part of the  
799 variation in the advance rates of NN9 and North Chongtar are due to these uncertainties rather than  
800 real variability.

801

802 With the exception of the Planet data, the uncertainty of the velocity measured over stable terrain  
803 by all sensors is one or two orders of magnitude smaller than the maximum displacement observed  
804 on the glacier along the centreline, even for the two small glaciers NN9 and North Chongtar. For  
805 them, cloud cover has been identified as a major challenge for optical sensors. In fact, the selection  
806 of the satellite pair prioritized the reduction of cloud cover on South Chongtar rather than NN9 and  
807 North Chongtar, which were rarely cloud-free. Hence, it is not only spatial resolution that is re-  
808 sponsible for data limitations.

809

810 In general, the uncertainties of glacier flow velocity measurements are mainly related to co-  
811 registration accuracy, orthorectification, the time interval between image pairs, surface conditions  
812 (shadow, snow, etc.) and the spatial resolution of the images. The larger the time window between  
813 two pairs, the smaller the uncertainty of the measured velocity. Despite the higher resolution, the  
814 uncertainty is higher for Planet than for Sentinel-2. For Sentinel-2, the orthorectification error is  
815 minimized because the imagery comes from the same relative orbit (Kääb et al., 2016). On the  
816 contrary, we have different orbital paths between Planet image pairs and therefore further geomet-  
817 ric corrections may be needed to minimize this error, as also suggested by Kääb et al. (2017) and  
818 Millan et al. (2019). Also the very small stable terrain uncertainties of TSX are likely due to the  
819 accurate co-registration of the image pairs.

820

821 The observed elevation changes exceed the DEM elevation uncertainties by an order of magnitude  
822 or more, which makes our elevation change analyses very robust. For volume change studies, data  
823 gaps in the DEMs and remaining blunders/bias from clouds or other sources cause greater uncer-  
824 tainties than the elevation uncertainties themselves (McNabb et al. 2019). Data gaps occur, how-  
825 ever, mostly in the accumulation areas due to reduced contrast over snow, more persistent cloud  
826 cover and steeper terrain. Moreover, surface elevation tends to change much less here than it is the  
827 case for the tongues, and uncertainties might become as large as the changes. The elevation accu-  
828 racy of the ICESat-2 ATL03 product is clearly superior to all DEMs analysed within this study.

829

830

## 831 **7. Conclusions**

832

833 We have identified and presented an analysis of three glacier surges in the central Karakoram, all  
834 taking place in the same region but with very different characteristics and possibly forcing mecha-  
835 nisms. South Chongtar showed advance rates of more than  $10 \text{ km y}^{-1}$ , velocities up to  $30 \text{ m d}^{-1}$  and



836 surface elevations rose by 200 m. The three times smaller North Chongtar has a slow and almost-  
837 linear increase of advance rates (up to  $500 \text{ m y}^{-1}$ ), flow velocities below  $1 \text{ m d}^{-1}$  and elevation in-  
838 creases of up to 100 m. The even smaller glacier NN9 changed from a slow advance to a full surge  
839 within a year, reaching advance rates higher than  $1 \text{ km y}^{-1}$ , but showing the typical surface lower-  
840 ing higher up only recently. Total length changes reached between 2 and 2.7 km for the three glac-  
841 iers and the size of NN9 changed by more than 20%. For South Chongtar, maximum flow veloci-  
842 ties are found near its southern boundary rather than in the centre.

843  
844 At first glance, the surge of South Chongtar clearly resembles the classical Alaska type surge (hy-  
845 drologically controlled), whereas North Chongtar and NN9 better fit to the Svalbard type (thermal-  
846 ly controlled). However, the summer onset and slow velocity decay of the South Chongtar surge  
847 and the sudden change in frontal advance rates of NN9 hint to the respective other type, resulting  
848 in a change of characteristics. North Chongtar has not changed type but surge onset is difficult to  
849 determine as advance rates increased linearly, morphological changes developed slowly and a 50-  
850 year advance might also be called a surge. When the definition of a surge is stricter, we would as-  
851 sign the surge onset of NN9, North and South Chongtar to 2017, 2005-2010 and August 2019, re-  
852 spectively. We speculate that the thin, lower part of South Chongtar was cold ice frozen to the bed,  
853 reducing possibilities for the terminus to advance and causing basal pressure to strongly increase.

854  
855 The sensor intercomparison revealed that Landsat 8 and Sentinel-2 are difficult to be used jointly  
856 for determination of geometric changes as their geolocation differs ( $>30 \text{ m}$ ). Flow velocities  
857 agreed well across sensors for South Chongtar, except for Sentinel-1 that had problems due to its  
858 narrow tongue (800 m). However, the backscatter intensity images provided a time-series of surge  
859 evolution at a near constant interval that is undisturbed by clouds. At the two smaller glaciers NN9  
860 and North Chongtar, the optical sensors still provided reasonable and consistent flow velocities,  
861 but limits due to spatial resolution and cloud cover became visible (more noise). The TerraSAR-X  
862 acquisitions in StripMap mode revealed by far the best results and depicted the surge of North  
863 Chongtar accurately.

864  
865 After proper co-registration, all DEMs provided useful results to track elevation and volume  
866 changes, independent of glacier size. The two SPOT DEMs from 2010 and 2015 suffered from  
867 artefacts at steep slopes, but the latter compared very well to the HMA-DEM. The high-resolution  
868 SPOT6 DEM from Oct 2020 had impressive quality and allowed an accurate calculation of the  
869 volume change of all glaciers up to this point in time. The very precise ICESat-2 elevation profiles  
870 provided additional information in space (glacier surface details) and time (between the DEMs)  
871 that matched well to the other datasets. The ASTER DEM time series missed detecting local  
872 changes of smaller glaciers, but provided a larger overview and complementary information on  
873 cumulative elevation changes shortly before the surge of South Chongtar started.



874

875 All three glaciers are still advancing and South Chongtar and NN9 are now colliding. The bulldoz-  
876 ing of the South Chongtar terminus into the down-wasting ice of Sarpo Laggo Glacier is already  
877 creating interesting morphological changes. North Chongtar might again reach the floor of the  
878 main valley as in the 1930s, but this could take some more years. We conclude that the past and  
879 further evolution of these and other glacier surges can be well observed from satellite data, at best  
880 by combing all available datasets.

881

### 882 **Supplement**

883 The supplement related to this article is available on-line at: TBD

884

### 885 **Author contributions**

886 F.P. detected the surges, lead the writing and analysed changes in extent and morphology. L.P.  
887 contributed equally, derived the optical velocity data and prepared all related tables and figures;  
888 D.T. derived and combined the elevation change data. All authors contributed to the writing, dis-  
889 cussion and editing of the text.

890

### 891 **Code and data availability**

892 Data processing has been performed using freely available (e.g. CIAS, MicMac, geopan-  
893 das/rasterio/shapely) or in-house software (for SAR offset-tracking). Also most of the datasets  
894 used here are freely available (e.g. Landsat, Sentinel-1/-2, Planet, ICESat-2, SRTM and HMA  
895 DEMs, glacier outlines), except TerraSAR-X data (ordered from DLR) and the SPOT2020 DEM  
896 (ordered from Airbus). The SPOT DEMs from 2010 and 2015 were provided by E. Berthier.

897

### 898 **Competing interests**

899 The authors declare that they have no conflict of interest.

900

### 901 **Acknowledgements**

902 This study has been performed in the framework of the ESA project Glaciers\_cci  
903 (4000127593/19/I-NB). We thank Etienne Berthier for providing the SPOT 2010 and 2015 DEMs.  
904 We also acknowledge free access to Sentinel-1 and -2 data from Copernicus, Landsat from USGS,  
905 Planet from Planet, the SRTM DEM from USGS, the HMA DEM from NSIDC, and glacier out-  
906 lines from GLIMS. This study would not have been possible otherwise.

907

### 908 **Financial support**

909 This study has been supported by the ESA project Glaciers\_cci (grant no. 4000127593/19/I-NB).

910

911



912

913 **References**

914

915 Bazai, N. A., Cui, P., Carling, P. A., Wang, H., Hassan, J., Liu, D., Zhang, G., and Jin, W.: In-  
916 creasing glacial lake outburst flood hazard in response to surge glaciers in the Karakoram,  
917 Earth-Science Reviews, 212, 103432, <https://doi.org/10.1016/j.earscirev.2020.103432>, 2021.

918 Berthier, E. and Brun, F.: Karakoram geodetic glacier mass balances between 2008 and 2016: per-  
919 sistence of the anomaly and influence of a large rock avalanche on Siachen Glacier, J. Glaciol.,  
920 65, 494–507, <https://doi.org/10.1017/jog.2019.32>, 2019.

921 Bhambri, R., Hewitt, K., Kawishwar, P., and Pratap, B.: Surge-type and surge-modified glaciers in  
922 the Karakoram, Sci Rep, 7, 15391, <https://doi.org/10.1038/s41598-017-15473-8>, 2017.

923 Bhambri, R., Hewitt, K., Kawishwar, P., Kumar, A., Verma, A., Snehamani, Tiwari, S., and Misra,  
924 A.: Ice-dams, outburst floods, and movement heterogeneity of glaciers, Karakoram, Global and  
925 Planetary Change, 180, 100–116, <https://doi.org/10.1016/j.gloplacha.2019.05.004>, 2019.

926 Bhambri, R., Watson, C. S., Hewitt, K., Haritashya, U. K., Kargel, J. S., Pratap Shahi, A., Chand,  
927 P., Kumar, A., Verma, A., and Govil, H.: The hazardous 2017–2019 surge and river damming  
928 by Shispare Glacier, Karakoram, Sci Rep, 10, 4685, <https://doi.org/10.1038/s41598-020-61277-8>, 2020.

930 Bolch, T., Pieczonka, T., Mukherjee, K., and Shea, J.: Brief communication: Glaciers in the Hunza  
931 catchment (Karakoram) have been nearly in balance since the 1970s, The Cryosphere, 11,  
932 531–539, <https://doi.org/10.5194/tc-11-531-2017>, 2017.

933 Brun, F., Berthier, E., Wagnon, P., Käab, A., and Treichler, D.: A spatially resolved estimate of  
934 High Mountain Asia glacier mass balances from 2000 to 2016, Nature Geosci, 10, 668–673,  
935 <https://doi.org/10.1038/ngeo2999>, 2017.

936 Copland, L., Sylvestre, T., Bishop, M. P., Shroder, J. F., Seong, Y. B., Owen, L. A., Bush, A., and  
937 Kamp, U.: Expanded and Recently Increased Glacier Surging in the Karakoram, Arctic, Ant-  
938 arctic, and Alpine Research, 43, 503–516, <https://doi.org/10.1657/1938-4246-43.4.503>, 2011.

939 Debella-Gilo M., and Käab, A.: Locally adaptive template sizes for matching repeat images of  
940 Earth surface mass movements. ISPRS Journal of Photogrammetry and Remote Sensing, 69,  
941 10–28, <https://doi.org/10.1016/j.isprsjprs.2012.02.002>, 2012.

942 Dehecq, A., Gourmelen, N., and Trouve, E.: Deriving large-scale glacier velocities from a com-  
943 plete satellite archive: Application to the Pamir–Karakoram–Himalaya, Remote Sensing of  
944 Environment, 162, 55–66, <https://doi.org/10.1016/j.rse.2015.01.031>, 2015.

945 Dunse, T., Schellenberger, T., Hagen, J.O., Käab, A., Schuler, T.V., and Reijmer, C.H.: Glacier-  
946 surge mechanisms promoted by a hydro-thermodynamic feedback to summer melt, The Cry-  
947 osphere, 9, 197–215, <https://doi.org/10.5194/tc-9-197-2015>, 2015.

948 Farinotti, D., Immerzeel, W. W., de Kok, R. J., Quincey, D. J., and Dehecq, A.: Manifestations and  
949 mechanisms of the Karakoram glacier Anomaly, Nat. Geosci., 13, 8–16,



- 950 <https://doi.org/10.1038/s41561-019-0513-5>, 2020.
- 951 Gardelle, J., Berthier, E., and Arnaud, Y.: Impact of resolution and radar penetration on glacier  
952 elevation changes computed from DEM differencing, *J. Glaciol.*, 58, 419–422,  
953 <https://doi.org/10.3189/2012JoG11J175>, 2012.
- 954 Gardelle, J., Berthier, E., Arnaud, Y., and Käab, A.: Region-wide glacier mass balances over the  
955 Pamir-Karakoram-Himalaya during 1999–2011, *The Cryosphere*, 7, 1263–1286,  
956 <https://doi.org/10.5194/tc-7-1263-2013>, 2013.
- 957 Gillies, S. et al.: Rasterio: geospatial raster I/O for Python programmers, Software from  
958 <https://github.com/Toblerity/Shapely>, 2021a.
- 959 Gillies, S. et al.: Shapely: manipulation and analysis of geometric objects, Software from  
960 <https://github.com/mapbox/rasterio>, 2021b.
- 961 Goerlich, F., Bolch, T., and Paul, F.: More dynamic than expected: an updated survey of surging  
962 glaciers in the Pamir, *Earth Syst. Sci. Data*, 12, 3161–3176, [https://doi.org/10.5194/essd-12-](https://doi.org/10.5194/essd-12-3161-2020)  
963 [3161-2020](https://doi.org/10.5194/essd-12-3161-2020), 2020.
- 964 Hewitt, K.: Tributary glacier surges: an exceptional concentration at Panmah Glacier, Karakoram  
965 Himalaya, *J. Glaciol.*, 53, 181–188, <https://doi.org/10.3189/172756507782202829>, 2007.
- 966 Hugonnet, R., McNabb, R., Berthier, E., Menounos, B., Nuth, C., Girod, L., Farinotti, D., Huss,  
967 M., Dussailant, I., Brun, F., and Käab, A.: Accelerated global glacier mass loss in the early  
968 twenty-first century, *Nature*, 592, 726–731, <https://doi.org/10.1038/s41586-021-03436-z>, 2021.
- 969 Iturrizaga, L.: New observations on present and prehistorical glacier-dammed lakes in the  
970 Shimshal valley (Karakoram Mountains), *Journal of Asian Earth Sciences*, 25, 545–555,  
971 <https://doi.org/10.1016/j.jseaes.2004.04.011>, 2005.
- 972 Jarvis, A., Reuter, H. I., Nelson, A., Guevara, E.: Hole-filled seamless SRTM data V4, Interna-  
973 tional Centre for Tropical Agriculture (CIAT) [dataset], <https://srtm.csi.cgiar.org>, 2008.
- 974 Jiskoot, H.: Glacier surging, in: *Encyclopedia of Snow, Ice and Glaciers*, edited by: Singh, V. P.,  
975 Springer, Dordrecht, Netherlands, pp. 415–428.
- 976 Jordahl, K., et al.: geopandas / geopandas: v0.9. Software from:  
977 <http://doi.org/10.5281/zenodo.4569086>, 2021.
- 978 Käab, A. and Vollmer, M.: Surface geometry, thickness changes and flow fields on creeping  
979 mountain permafrost: automatic extraction by digital image analysis. *Permafrost Periglac.*, 11,  
980 315–326, [https://doi.org/10.1002/1099-1530\(200012\)11:4<315::AID-PPP365>3.0.CO;2-J](https://doi.org/10.1002/1099-1530(200012)11:4<315::AID-PPP365>3.0.CO;2-J), 2000.
- 981 Käab, A., Berthier, E., Nuth, C., Gardelle, J., and Arnaud, Y.: Contrasting patterns of early twenty-  
982 first-century glacier mass change in the Himalayas, *Nature*, 488, 495–498,  
983 <https://doi.org/10.1038/nature11324>, 2012.
- 984 Käab, A., Winsvold, S.H., Altena, B., Nuth, C., Nagler, T., and Wuite, J.: Glacier remote sensing  
985 using Sentinel-2. Part I: Radiometric and geometric performance, and application to ice veloci-  
986 ty, *Remote Sensing*, 8(7), 598, <https://doi.org/10.3390/rs8070598>, 2016.
- 987 Käab, A., Altena, B., and Mascaro, J.: Coseismic displacements of the 14 November 2016 Mw 7.8



- 988 Kaikoura, New Zealand, earthquake using the Planet optical cubesat constellation, *Nat. Haz-*  
989 *ards Earth Syst. Sci.*, 17, 627–639, <https://doi.org/10.5194/nhess-17-627-2017>, 2017.
- 990 King, O., Bhattacharya, A., and Bolch, T.: The presence and influence of glacier surging around  
991 the Geladandong ice caps, North East Tibetan Plateau, *Advances in Climate Change Research*,  
992 12, 299–312, <https://doi.org/10.1016/j.accre.2021.05.001>, 2021.
- 993 Leclercq, P. W., Käab, A., and Altena, B.: Brief communication: Detection of glacier surge activi-  
994 ty using cloud computing of Sentinel-1 radar data, *The Cryosphere*, 15, 4901–4907,  
995 <https://doi.org/10.5194/tc-15-4901-2021>, 2021.
- 996 Leinss, S. and Bernhard, P.: TanDEM-X: Deriving InSAR Height Changes and Velocity Dynamics  
997 of Great Aletsch Glacier, *IEEE J. Sel. Top. Appl. Earth Observations Remote Sensing*, 14,  
998 4798–4815, <https://doi.org/10.1109/JSTARS.2021.3078084>, 2021.
- 999 Lv, M., Guo, H., Lu, X., Liu, G., Yan, S., Ruan, Z., Ding, Y., and Quincey, D. J.: Characterizing  
1000 the behaviour of surge- and non-surge-type glaciers in the Kingata Mountains, eastern Pamir,  
1001 from 1999 to 2016, *The Cryosphere*, 13, 219–236, <https://doi.org/10.5194/tc-13-219-2019>,  
1002 2019.
- 1003 Lv, M., Guo, H., Yan, J., Wu, K., Liu, G., Lu, X., Ruan, Z., and Yan, S.: Distinguishing Glaciers  
1004 between Surging and Advancing by Remote Sensing: A Case Study in the Eastern Karakoram,  
1005 *Remote Sensing*, 12, 2297, <https://doi.org/10.3390/rs12142297>, 2020.
- 1006 Mayer, C., Fowler, A. C., Lambrecht, A., and Scharrer, K.: A surge of North Gasherbrum Glacier,  
1007 Karakoram, China, 57, 904–916, <https://doi.org/10.3189/002214311798043834>, 2011.
- 1008 Markus, T., Neumann, T., Martino, A., Abdalati, W., Brunt, K., Csatho, B., Farrell, S., Fricker, H.,  
1009 Gardner, A., Harding, D., Jasinski, M., Kwok, R., Magruder, L., Lubin, D., Luthcke, S., Mori-  
1010 son, J., Nelson, R., Neuenschwander, A., Palm, S., Popescu, S., Shum, C.K., Schutz, B.E.,  
1011 Smith, B., Yang, Y., and Zwally, J.: The Ice, Cloud, and land Elevation Satellite-2 (ICESat-2):  
1012 Science requirements, concept, and implementation. *Remote Sensing of Environment*, 190,  
1013 260–273, <https://doi.org/10.1016/j.rse.2016.12.029>, 2017.
- 1014 Maussion, F., Scherer, D., Mölg, T., Collier, E., Curio, J., and Finkelnburg, R.: Precipitation Sea-  
1015 sonality and Variability over the Tibetan Plateau as Resolved by the High Asia Reanalysis, 27,  
1016 1910–1927, <https://doi.org/10.1175/JCLI-D-13-00282.1>, 2014.
- 1017 McNabb, R., Nuth, C., Käab, A., and Girod, L.: Sensitivity of glacier volume change estimation to  
1018 DEM void interpolation, *The Cryosphere*, 13, 895–910, [https://doi.org/10.5194/tc-13-895-](https://doi.org/10.5194/tc-13-895-2019)  
1019 [2019](https://doi.org/10.5194/tc-13-895-2019), 2019.
- 1020 Millan, R., Mouginit, J., Rabatel, A., Jeong, S., Cusicanqui, D., Derkacheva, A., and Chekki, M.:  
1021 Mapping Surface Flow Velocity of Glaciers at Regional Scale Using a Multiple Sensors Ap-  
1022 proach, *Remote Sensing*, 11, 2498, <https://doi.org/10.3390/rs11212498>, 2019.
- 1023 Murray, T., T. Strozzi, A. Luckman, H. Jiskoot, and P. Christakos, Is there a single surge mecha-  
1024 nism? Contrasts in dynamics between glacier surges in Svalbard and other regions, *J. Geophys.*  
1025 *Res.*, 108(B5), 2237, <https://doi.org/10.1029/2002JB001906>, 2003.





- 1026 Neumann, T. A., A. Brenner, D. Hancock, J. Robbins, J. Saba, K. Harbeck, A. Gibbons, J. Lee, S.  
1027 B. Luthcke, T. Rebold, et al. 2021. *ATLAS/ICESat-2 L2A Global Geolocated Photon Data,*  
1028 *Version 4.* Boulder, Colorado USA. NASA National Snow and Ice Data Center Distributed  
1029 Active Archive Center. <https://doi.org/10.5067/ATLAS/ATL03.004>. [Last accessed 16 Oc-  
1030 tober 2021].
- 1031 Neumann, T.: Technical Specs – ICESat-2 Ground Tracks, [https://icesat-](https://icesat-2.gsfc.nasa.gov/science/specs#:~:text=Over%20the%20polar%20areas%20and.measure%20more%20of%20Earth's%20forests)  
1032 [2.gsfc.nasa.gov/science/specs#:~:text=Over%20the%20polar%20areas%20and.measure%20m-](https://icesat-2.gsfc.nasa.gov/science/specs#:~:text=Over%20the%20polar%20areas%20and.measure%20more%20of%20Earth's%20forests)  
1033 [ore%20of%20Earth's%20forests](https://icesat-2.gsfc.nasa.gov/science/specs#:~:text=Over%20the%20polar%20areas%20and.measure%20more%20of%20Earth's%20forests), 2019 [last access: 15 April 2021].
- 1034 NSIDC: ATL06 Known Issues (V03), [https://nsidc.org/sites/nsidc.org/files/technical-](https://nsidc.org/sites/nsidc.org/files/technical-references/ICESat2_ATL06_Known_issues_v003_Sept2020.pdf)  
1035 [references/ICESat2\\_ATL06\\_Known\\_issues\\_v003\\_Sept2020.pdf](https://nsidc.org/sites/nsidc.org/files/technical-references/ICESat2_ATL06_Known_issues_v003_Sept2020.pdf), 2020 [last access: 3 Decem-  
1036 ber 2020].
- 1037 Nuth, C., Gilbert, A., Köhler, A., McNabb, R., Schellenberger, T., Sevestre, H., Weidle, C., Girod,  
1038 L., Luckman, A., and Käab, A.: Dynamic vulnerability revealed in the collapse of an Arctic  
1039 tidewater glacier, *Scientific Reports*, 9, 5541, [https://doi.org/ 10.1038/s41598-019-41117-0](https://doi.org/10.1038/s41598-019-41117-0),  
1040 2019.
- 1041 Obu, J., Westermann, S., Bartsch, A., Berdnikov, N., Christiansen, H. H., Dashtseren, A.,  
1042 Delaloye, R., Elberling, B., Etzelmüller, B., Kholodov, A., Khomutov, A., Käab, A., Leibman,  
1043 M. O., Lewkowicz, A. G., Panda, S. K., Romanovsky, V., Way, R. G., Westergaard-Nielsen,  
1044 A., Wu, T., Yamkhin, J., and Zou, D.: Northern Hemisphere permafrost map based on TTOP  
1045 modelling for 2000–2016 at 1 km<sup>2</sup> scale, *Earth-Science Reviews*, 193, 299–316,  
1046 <https://doi.org/10.1016/j.earscirev.2019.04.023>, 2019.
- 1047 Paul, F.: Revealing glacier flow and surge dynamics from animated satellite image sequences: ex-  
1048 amples from the Karakoram, *The Cryosphere*, 9, 2201–2214, [https://doi.org/10.5194/tc-9-](https://doi.org/10.5194/tc-9-2201-2015)  
1049 [2201-2015](https://doi.org/10.5194/tc-9-2201-2015), 2015.
- 1050 Paul, F.: A 60-year chronology of glacier surges in the central Karakoram from the analysis of sat-  
1051 ellite image time-series, *Geomorphology*, 352, 106993,  
1052 <https://doi.org/10.1016/j.geomorph.2019.106993>, 2020.
- 1053 Paul, F., Bolch, T., Briggs, K., Käab, A., McMillan, M., McNabb, R., Nagler, T., Nuth, C.,  
1054 Rastner, P., Strozzi, T., and Wuite, J.: Error sources and guidelines for quality assessment of  
1055 glacier area, elevation change, and velocity products derived from satellite data in the Glaci-  
1056 ers\_cci project, *Remote Sensing of Environment*, 203, 256–275,  
1057 <https://doi.org/10.1016/j.rse.2017.08.038>, 2017.
- 1058 Paul, F., Strozzi, T., Schellenberger, T., and Käab, A.: The 2015 Surge of Hispar Glacier in the  
1059 Karakoram, *Remote Sensing*, 9, 888, <https://doi.org/10.3390/rs9090888>, 2017.
- 1060 Paul, F., Winsvold, S., Käab, A., Nagler, T., and Schwaizer, G.: Glacier Remote Sensing Using  
1061 Sentinel-2. Part II: Mapping Glacier Extents and Surface Facies, and Comparison to Landsat 8,  
1062 *Remote Sensing*, 8, 575, <https://doi.org/10.3390/rs8070575>, 2016.
- 1063 Pfeifer, N., Mandlbürger, G., Otepka, J., and Karel, W.: OPALS – A framework for Airborne La-





- 1064 ser Scanning data analysis, *Computers, Environment and Urban Systems*, 45, 125–136,  
1065 <https://doi.org/10.1016/j.compenvurbsys.2013.11.002>, 2014.
- 1066 Quincey, D. J., Glasser, N. F., Cook, S. J., and Luckman, A.: Heterogeneity in Karakoram glacier  
1067 surges, *J. Geophys. Res. Earth Surf.*, 120, 1288–1300, <https://doi.org/10.1002/2015JF003515>,  
1068 2015.
- 1069 Rankl, M. and Braun, M.: Glacier elevation and mass changes over the central Karakoram region  
1070 estimated from TanDEM-X and SRTM/X-SAR digital elevation models, *Ann. Glaciol.*, 57,  
1071 273–281, <https://doi.org/10.3189/2016AoG71A024>, 2016.
- 1072 Rankl, M., Kienholz, C., and Braun, M.: Glacier changes in the Karakoram region mapped by mul-  
1073 timission satellite imagery, *The Cryosphere*, 8, 977–989, [https://doi.org/10.5194/tc-8-977-](https://doi.org/10.5194/tc-8-977-2014)  
1074 [2014](https://doi.org/10.5194/tc-8-977-2014), 2014.
- 1075 Rashid, I., Majeed, U., Jan, A., and Glasser, N. F.: The January 2018 to September 2019 surge of  
1076 Shisper Glacier, Pakistan, detected from remote sensing observations, *Geomorphology*, 351,  
1077 106957, <https://doi.org/10.1016/j.geomorph.2019.106957>, 2020.
- 1078 Raymond, C. F.: How do glaciers surge? A review, *J. Geophys. Res.*, 92, 9121,  
1079 <https://doi.org/10.1029/JB092iB09p09121>, 1987.
- 1080 Round, V., Leinss, S., Huss, M., Haemmig, C., and Hajnsek, I.: Surge dynamics and lake outbursts  
1081 of Kyagar Glacier, Karakoram, *The Cryosphere*, 11, 723–739, [https://doi.org/10.5194/tc-11-](https://doi.org/10.5194/tc-11-723-2017)  
1082 [723-2017](https://doi.org/10.5194/tc-11-723-2017), 2017.
- 1083 Rupnik, E., Daakir, M., and Pierrot Deseilligny, M.: MicMac – a free, open-source solution for  
1084 photogrammetry, *Open geospatial data, softw. stand.*, 2, 14, [https://doi.org/10.1186/s40965-](https://doi.org/10.1186/s40965-017-0027-2)  
1085 [017-0027-2](https://doi.org/10.1186/s40965-017-0027-2), 2017.
- 1086 Sakai, A.: Brief communication: Updated GAMDAM glacier inventory over high-mountain Asia,  
1087 *The Cryosphere*, 13, 2043–2049, <https://doi.org/10.5194/tc-13-2043-2019>, 2019.
- 1088 Sakai, A., Niumura, T., Fujita, K., Takenaka, S., Nagai, H., and Lamsal, D.: Climate regime of  
1089 Asian glaciers revealed by GAMDAM glacier inventory, *The Cryosphere*, 9, 865–880,  
1090 <https://doi.org/10.5194/tc-9-865-2015>, 2015.
- 1091 Sevestre, H. and Benn, D. I.: Climatic and geometric controls on the global distribution of surge-  
1092 type glaciers: implications for a unifying model of surging, *J. Glaciol.*, 61, 646–662,  
1093 <https://doi.org/10.3189/2015JG14J136>, 2015.
- 1094 Sharp, M.: Surging glaciers: behaviour and mechanisms, *Progress in Physical Geography: Earth*  
1095 *and Environment*, 12, 349–370, <https://doi.org/10.1177/030913338801200302>, 1988.
- 1096 Shean, D.E., Alexandrov, O., Moratto, Z., Smith, B.E., Joughin, I.R., Porter, C.C. and Morin, P. J.:  
1097 An automated, open-source pipeline for mass production of digital elevation models (DEMs)  
1098 from very high-resolution commercial stereo satellite imagery. *ISPRS Journal of Photogram-*  
1099 *metry and Remote Sensing*, 116, 101–117, <http://doi.org/10.1016/j.isprsjprs.2016.03.012>,  
1100 2016.
- 1101 Shean, D.: High Mountain Asia 8-meter DEM Mosaics Derived from Optical Imagery, Version 1,



- 1102 NASA NSIDC Distributed Active Archive Center, <https://doi.org/10.5067/KXOVQ9L172S2>,  
1103 2017, [last access: June 2021].
- 1104 Shipton, E., Spender, M., and Auden, J. B.: The Shaksgam Expedition, 1937, *The Geographical*  
1105 *Journal*, 91, 313, <https://doi.org/10.2307/1788187>, 1938.
- 1106 Smith, B., Fricker, H. A., Gardner, A., Siegfried, M. R., Adusumilli, S., Csathó, B. M., Holschuh,  
1107 N., Nilsson, J., Paolo, F.S., and the ICESat-2 Science Team: ATLAS/ICESat-2 L3A Land Ice  
1108 Height, Version 3, NASA NSIDC Distributed Active Archive Center [dataset],  
1109 <https://doi.org/10.5067/ATLAS/ATL06.003>, 2020, [last access: 3 December 2020].
- 1110 Steiner, J. F., Kraaijenbrink, P. D. A., Jiduc, S. G., and Immerzeel, W. W.: Brief communication:  
1111 The Khurdopin glacier surge revisited – extreme flow velocities and formation of a dammed  
1112 lake in 2017, *The Cryosphere*, 12, 95–101, <https://doi.org/10.5194/tc-12-95-2018>, 2018.
- 1113 Strozzi, T., Luckman, A., Murray, T., Wegmüller, U., and Werner, C. L.: Glacier motion estima-  
1114 tion using SAR offset-tracking procedures, *IEEE Trans. Geosci. Remote Sensing*, 40, 2384–  
1115 2391, <https://doi.org/10.1109/TGRS.2002.805079>, 2002.
- 1116 Strozzi, T., Paul, F., Wiesmann, A., Schellenberger, T., and Kääb, A.: Circum-Arctic Changes in  
1117 the Flow of Glaciers and Ice Caps from Satellite SAR Data between the 1990s and 2017, *Re-  
1118 mote Sensing*, 9, 947, <https://doi.org/10.3390/rs9090947>, 2017.
- 1119 USGS, Earth Resources Observation and Science (EROS) Center: USGS EROS Archive – Digital  
1120 Elevation - Shuttle Radar Topography Mission (SRTM) 1 Arc-Second Global [dataset],  
1121 <https://doi.org/10.5066/F7PR7TFT>, 2017, [last access: 2020].
- 1122 Wang, X., Shangguan, D., Li, D., and Anjum, M. N.: Spatiotemporal Variability of Velocity and  
1123 Influence of Glacier Thickness Using Landsat Imagery: Hunza River Basin, Karakoram  
1124 Range, *IEEE Access*, 9, 72808–72819, <https://doi.org/10.1109/ACCESS.2021.3078775>, 2021.
- 1125 Willis, M. J., Zheng, W., Durkin, W. J., Pritchard, M. E., Ramage, J. M., Dowdeswell, J. A., Ben-  
1126 ham, T. J., Bassford, R. P., Stearns, L. A., Glazovsky, A. F., Macheret, Y. Y., and Porter, C.  
1127 C.: Massive destabilization of an Arctic ice cap, *Earth and Planetary Science Letters*, 502,  
1128 146–155, <https://doi.org/10.1016/j.epsl.2018.08.049>, 2018.
- 1129 Wuite, J., Rott, H., Hetzenecker, M., Floricioiu, D., De Rydt, J., Gudmundsson, G. H., Nagler, T.,  
1130 and Kern, M.: Evolution of surface velocities and ice discharge of Larsen B outlet glaciers  
1131 from 1995 to 2013, *The Cryosphere*, 9, 957–969, <https://doi.org/10.5194/tc-9-957-2015>, 2015.
- 1132 Zhou, Y., Li, Z., and Li, J.: Slight glacier mass loss in the Karakoram region during the 1970s to  
1133 2000 revealed by KH-9 images and SRTM DEM, *J. Glaciol.*, 63, 331–342,  
1134 <https://doi.org/10.1017/jog.2016.142>, 2017.
- 1135
- 1136



1137 **Tables**

1138

1139 *Table 1: Characteristics of the three investigated glaciers using outlines modified from the*  
 1140 *GAMDAM2 glacier inventory (Sakai et al. 2019) and digitized in this study. Elevations refer to the*  
 1141 *SRTM DEM. Values given for ‘min/max’ refer to the minimum and maximum extent of a glacier*  
 1142 *shortly before and after a surge, respectively.*

	NN9	North Chongtar	South Chongtar
Size (min / max)	3.93 / 4.78 km <sup>2</sup>	9.16 / 10.15 km <sup>2</sup>	31.09 / 34.23 km <sup>2</sup>
Size change (km <sup>2</sup> / percent)	+0.85 km <sup>2</sup> / +21.6%	+0.99 km <sup>2</sup> / +10.9%	+3.14 km <sup>2</sup> / +10.0%
Elevation (highest / mean)	6450 / 5620 m	6810 / 5860 m	7230 / 5920 m
Lowest elevation (min / max)	4430 / 5075 m	4440 / 5015 m	4545 / 4400 m
Length (min / max)	3.25 / 5.5 km	4.75 / 6.8 km	14.4 / 17.1 km
Changes (min. elev. / length)	645 / 2250 m	575 / 2050 m	145 / 2700 m
Slope / Aspect	31.5 / SE	28.8 / NW	25.1 / NW
Previous surge	1961-1971	1920s	1966-68
Surge repeat cycle	40-50 y	90 y?	54 y
This surge	2000-today	1965-today	2020-today
Characteristics	Compact dual-basin valley glacier with prominent medial moraine	Dual-basin valley glacier with one major tributary forming a prominent medial moraine	Long and flat single-basin valley glacier with three tributaries (one resulting in a short medial moraine)

1143

1144

1145 *Table 2: Overview of the DEMs used to determine elevation changes of the glaciers in the study*  
 1146 *region and the additional ICESat-2 dataset.*

Nr.	Name (short)	Type	Reso- lution	Date	Source	Comments
1	SRTM 1	SAR	30 m	Feb. 2000	USGS, doi: 10.5066/f7pr7ftt	C-band w/ penetration
2	HMA-DEM	OPT	8 m	Feb-Aug. 2015	NSIDC, doi: 10.5067/KXOVQ9L172S2	7 months composite
3	SPOT 2010	OPT	30 m	31 Oct 2010	Gardelle et al. 20013	SPOT 5 HRS
4	SPOT 2015	OPT	30 m	13 Oct 2015	Berthier & Brun 2019	SPOT 6
5	SPOT 2020	OPT	10 m	20 Oct 2020	Ordered from Airbus	SPOT 6
6	ASTER	OPT	30 m	2000-2019	Hugonnet et al. 2021	5y elevation changes
7	ICESat-2	LIDAR	0.7 m	3.12. 2018 – 5.11.2020	NSIDC, nsidc.org/data/icesat-2/data-sets	Version 4, 14 tracks, over glaciers only

1147

1148

1149 *Table 3: Calculated volume changes (in km<sup>3</sup>) for six glaciers and different periods as obtained*  
 1150 *from the respective DEMs. Grey umbers in italics denote results that might be impacted by*  
 1151 *artefacts.*

Nr.	Glacier	Period	Gain	Loss	Total
1	South Chongtar	2015-2020	0.3444	-0.1760	0.1684
2	North Chongtar	2000-2020	0.0466	-0.0365	0.0102
3	NN9	2000-2020	0.0356	<i>-0.0017</i>	0.0339
4	NN8	2000-2010	0.0175	-0.0167	0.0008
5	NN7	2000-2010	0.0146	-0.0304	-0.0158
6	Sarpo Laggo	2000-2020	<i>0.0024</i>	-0.4708	-0.4684

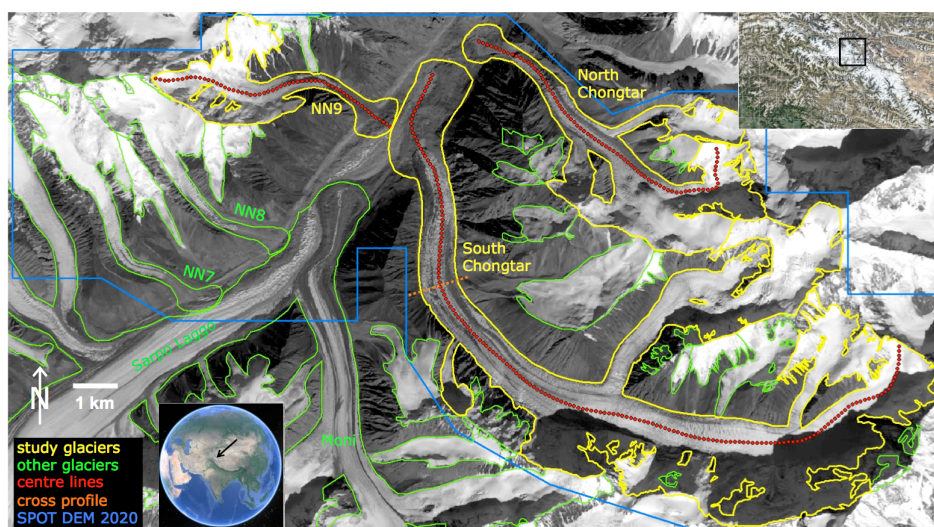
1152

1153



1154 **Figures**

1155

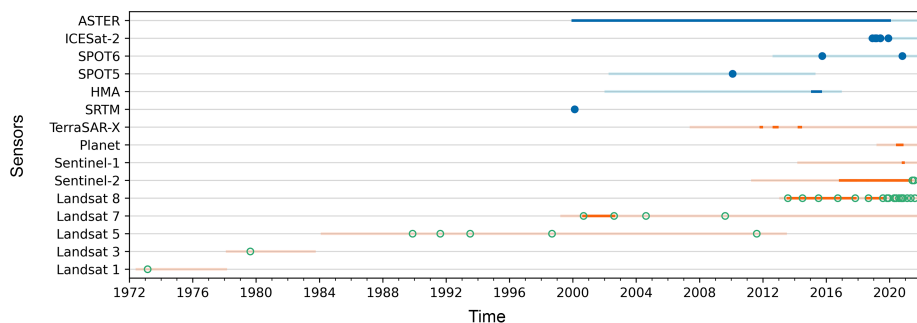


1156

1157 *Fig. 1: Overview of the study region showing the location of the Karakoram Mountains (inset,*  
 1158 *lower left) and of the study region (inset upper right), outlines of the investigated glaciers (yellow),*  
 1159 *other glaciers (green), centre lines (red), cross-profile line (orange) and extent of the SPOT 2020*  
 1160 *DEM perimeter (blue). The satellite image in the background is the panchromatic band from*  
 1161 *Landsat 8 acquired on 21 Oct 2020 (Landsat data: earthexplorer.usgs.gov), the two insets are*  
 1162 *screenshots from © Google Earth.*

1163

1164



1165

1166 *Figure 2. Timeline of the temporal coverage of the satellite sensors used (light line) and dates and*  
 1167 *time series selected for the analysis (lines or dots). Lines and dots in dark blue indicate the*  
 1168 *elevation change analysis, orange lines the velocity analysis, and green dots the glacier extents.*

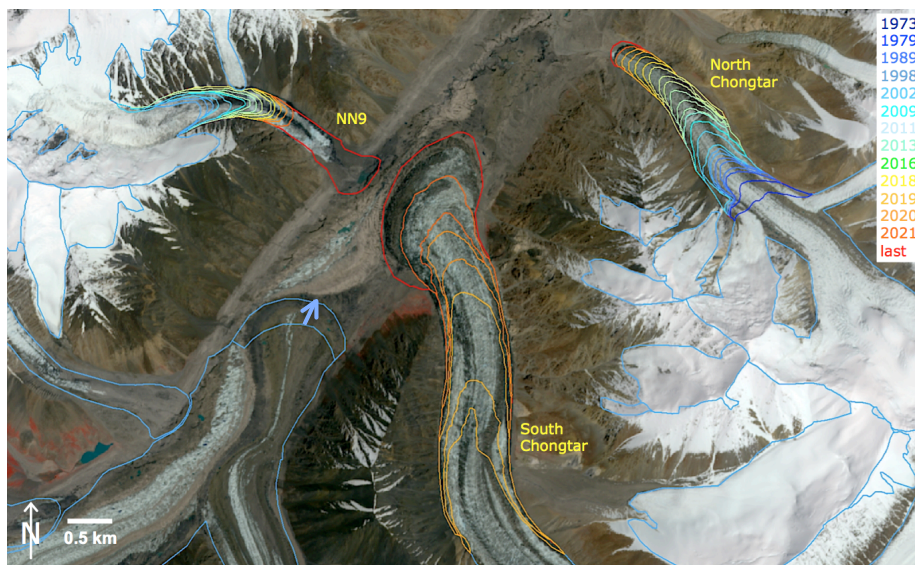
1169

1170

1171



1172

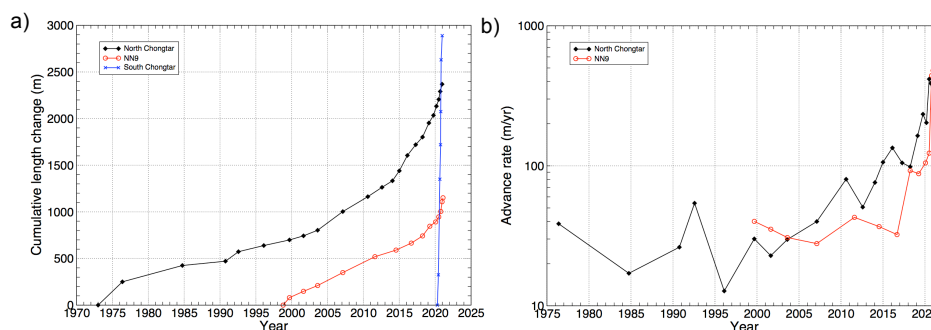


1173

1174 Fig. 3: Temporal evolution (colour-coded dates) of glacier extent for the three glaciers (NN9,  
1175 North Chongtar, South Chongtar) investigated here. For comparison, the displacement of the  
1176 terminal lobe of Moni Glacier from 2000 to 2020 is also shown (arrow). ‘Last’ is referring to 30  
1177 September 2021. Background: Sentinel-2 image acquired on 16 July 2021 with bands 8/4/3 as  
1178 RGB (Copernicus Sentinel data 2021).

1179

1180



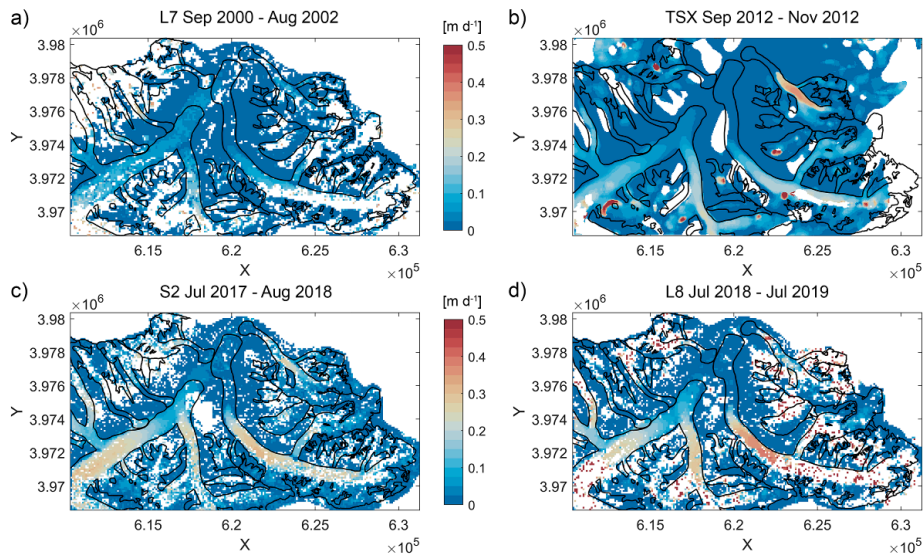
1181

1182 Fig. 4: Terminus changes for the investigated glaciers. a) Cumulative length changes (the retreat  
1183 phase of South Chongtar before 2020 is not shown), b) advance rates.

1184

1185

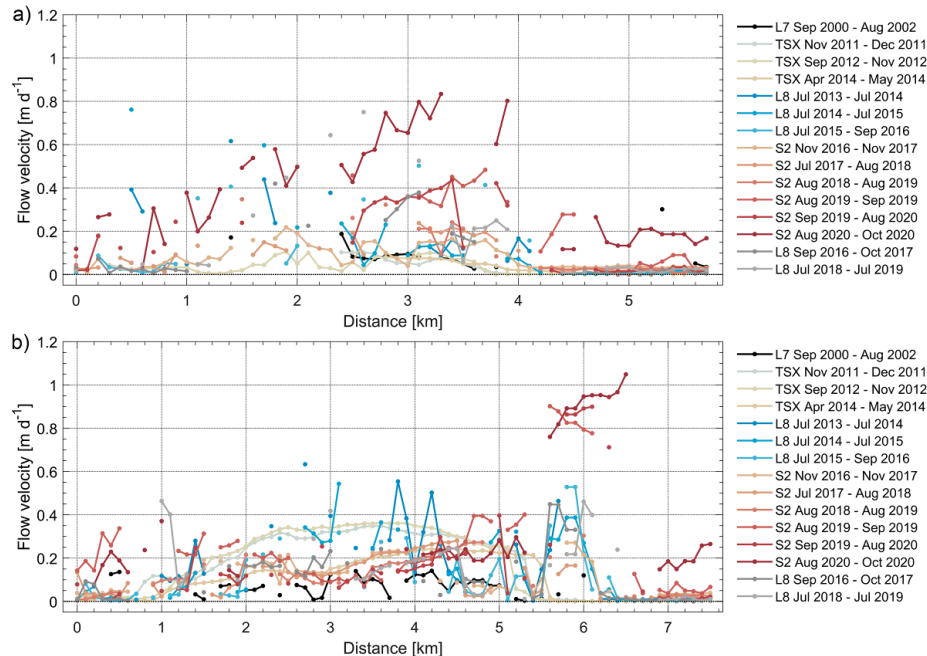




1186

1187 *Fig. 5: Temporal evolution of 2D surface flow velocities for the three glaciers before 2020 derived*  
 1188 *from a) Landsat 7, b) TerraSAR-X, c) Sentinel-2, and d) Landsat 8. The dates of the compared*  
 1189 *images are given at the top of each panel.*

1190

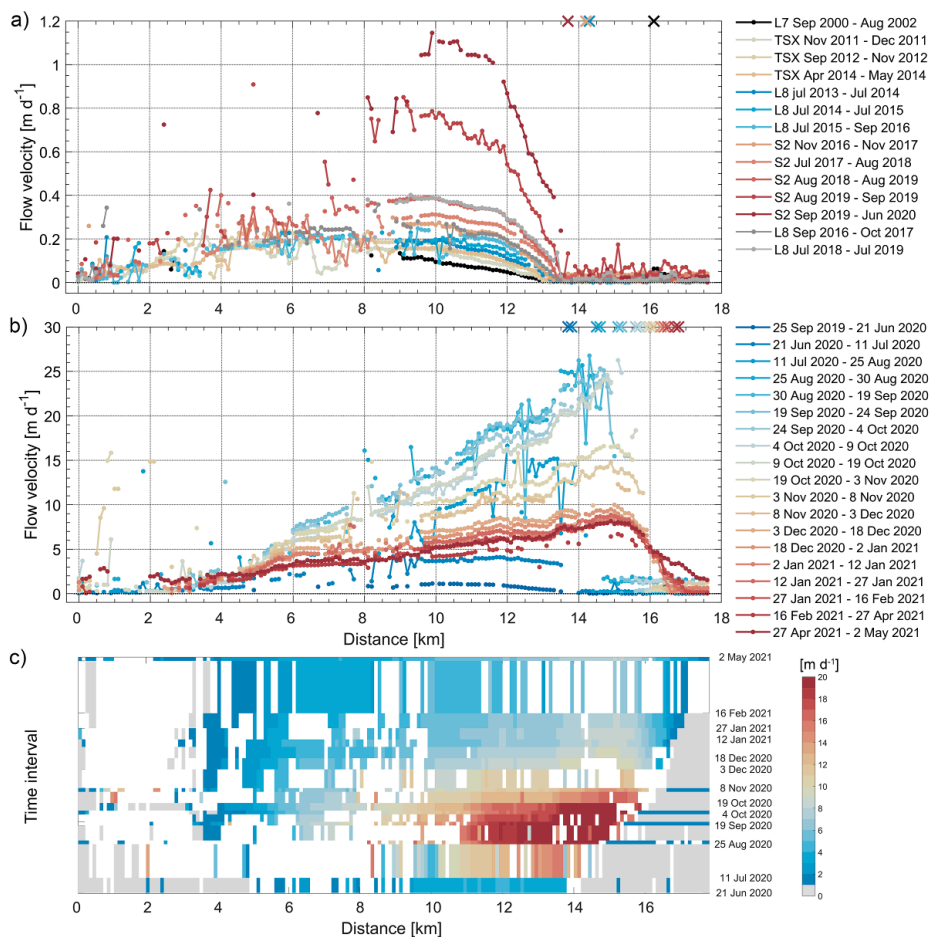


1191

1192 *Fig. 6: Temporal evolution of 1D flow velocities along a centre-line starting at the highest point of*  
 1193 *each glacier for a) glacier NN9 and b) North Chongtar. Satellite names: L7/L8: Landsat 7/8, TSX:*  
 1194 *Terra-SAR-X, S2: Sentinel-2.*



1195



1196

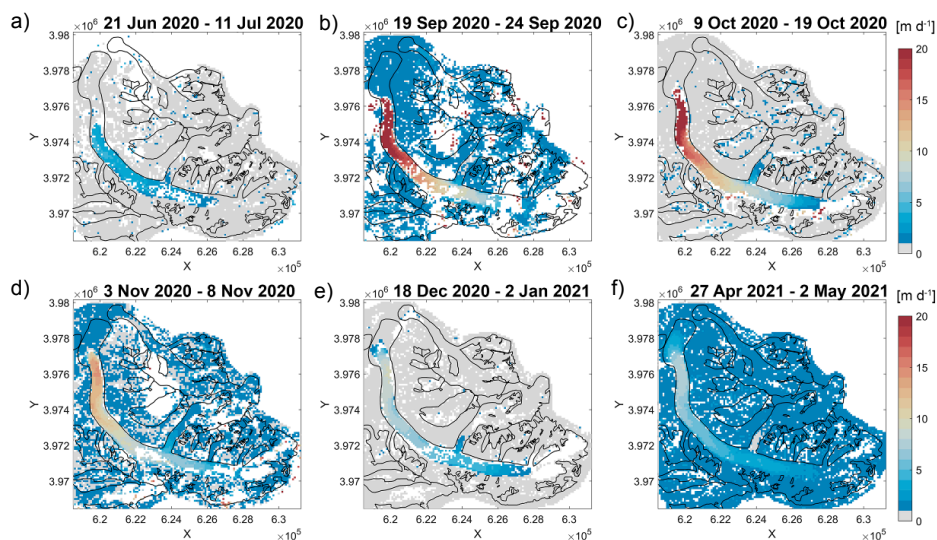
1197 *Fig. 7: Temporal evolution of flow velocities for South Chongtar Glacier from its highest point to*  
1198 *its terminus, its location is indicated by an 'x' at the top of panels a) and b). a) Pre-surge values*  
1199 *along the centre-line as derived from different satellites (names see Fig. 6). b) As a) but during the*  
1200 *surge and derived from Sentinel-2 only, c) Hovmöller diagram of the surge phase. In this plot grey*  
1201 *values are below 1 m d<sup>-1</sup>, white indicates no data.*

1202

1203



1204

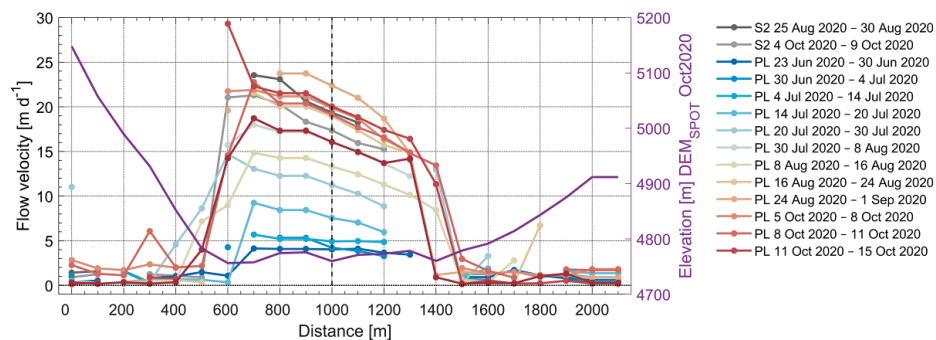


1205

1206 *Fig. 8: Temporal evolution of 2D flow velocities for South Chongtar Glacier during its surge as*  
 1207 *derived from Sentinel-2. The dates of the respective Sentinel-2 pairs are given at the top of each*  
 1208 *panel.*

1209

1210

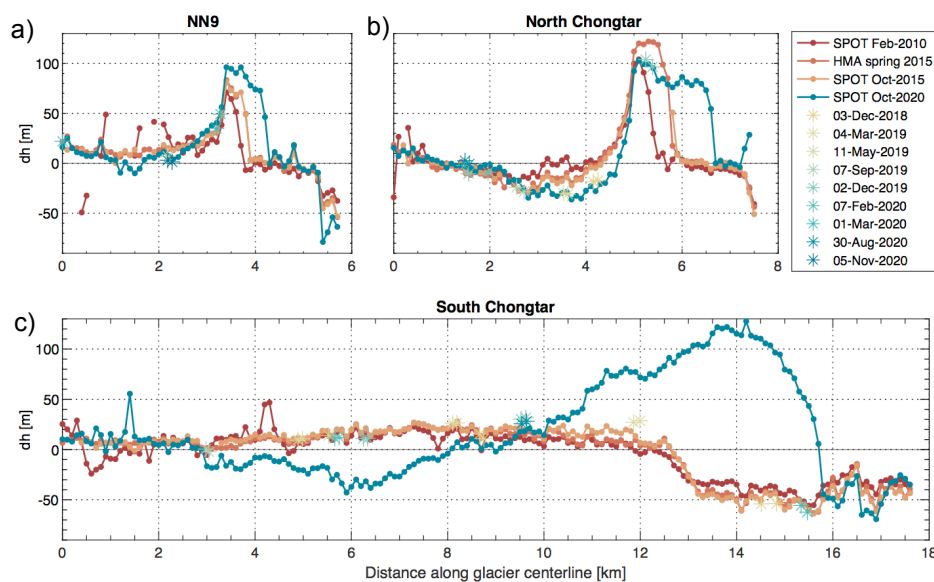


1211

1212 *Fig. 9: Cross-profile surface flow velocities for South Chongtar Glacier derived from Planet and*  
 1213 *comparison with Sentinel-2. The vertical dash line indicates the location of the centerline.*

1214

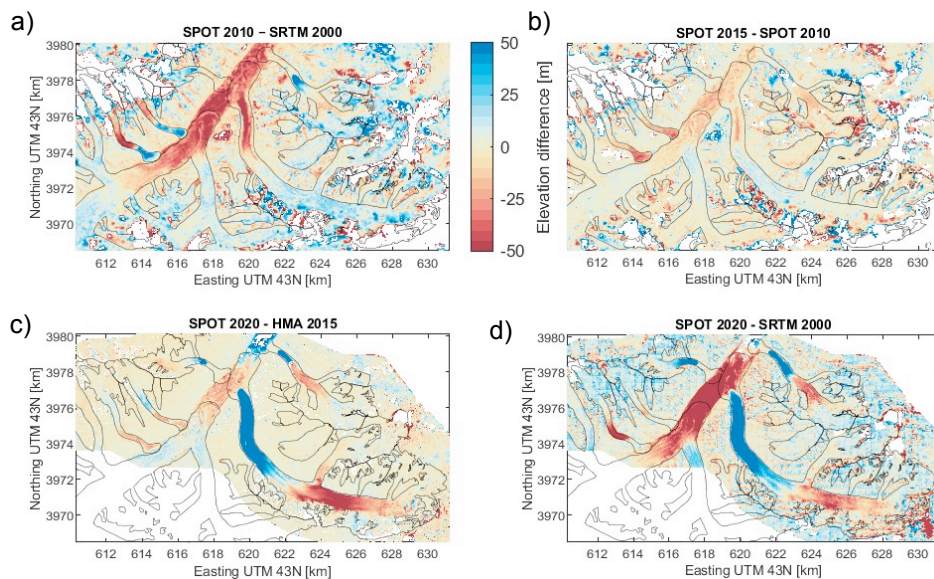




1215

1216 *Fig. 10: Elevation differences along the glacier centerlines in respect to the SRTM DEM from*  
 1217 *2000 for the three investigated glaciers, namely a) NN9, b) North Chongtar, and c) South*  
 1218 *Chongtar glaciers. The star (\*) markers and dates in the legend correspond to ICESat-2 elevation*  
 1219 *differences in respect to the SRTM DEM. Note that due to the different track locations, only some*  
 1220 *of the dates shown in the legend are present in each panel.*

1221



1222

1223 *Fig. 11: 2D elevation difference maps over the study region. a) SPOT 2010 – SRTM 2000, b)*  
 1224 *SPOT 2015 – SPOT 2010, c) SPOT 2020 – HMA 2015, d) SPOT 2020 – SRTM 2000. A*  
 1225 *comparison between the SPOT 2015 and the HMA DEM from 2015 is shown in Fig. S13.*